Wavelet-Based Blind Deconvolution and Denoising of Ultrasound Scans for Non-Destructive Test Applications

by

Jason Richard Benjamin Taylor

A Thesis submitted to the Faculty of Graduate Studies of
The University of Manitoba
in partial fulfillment of the requirement of the degree of

MASTER OF SCIENCE

Department of Electrical and Computer Engineering
University of Manitoba
Winnipeg

Abstract

A novel technique for blind deconvolution of ultrasound is introduced. Existing deconvolution techniques for ultrasound such as cepstrum-based methods and the work of Adam and Michailovich – based on Discrete Wavelet Transform (DWT) shrinkage of the log-spectrum – exploit the smoothness of the pulse log-spectrum relative to the reflectivity function to estimate the pulse. To reduce the effects of non-stationarity in the ultrasound signal on both the pulse estimation and deconvolution, the log-spectrum is time-localized and represented as the Continuous Wavelet Transform (CWT) log-scalogram in the proposed technique. The pulse CWT coefficients are estimated via DWT shrinkage of the log-scalogram and are then deconvolved by wavelet-domain Wiener filtering. Parameters of the technique are found by heuristic optimization on a training set with various quality metrics: entropy, autocorrelation 6-dB width and fractal dimension. The technique is further enhanced by using different CWT wavelets for estimation and deconvolution, similar to the WienerChop method.

Acknowledgments

I would like to thank my advisor Dr. Gabriel Thomas for his guidance and encouragement throughout my studies. His impact on the quality and enjoyment of my education cannot be overstated. I would also like to thank Dr. Boyd McCurdy and Dr. Ekram Hossain for their participation on my examining committee.

Funding for this work was provided by the Natural Sciences and Engineering Research Council of Canada through a Collaborative Research and Development Grant co-sponsored by Manitoba Hydro and CancerCare Manitoba.

Jose Mijares Chan was of tremendous help in performing experiments as well as discussing ideas and problems both technical and nontechnical in nature. Thanks, Jose.

I would also like to thank my parents for their support and enthusiasm throughout my studies. Finally, I would like to thank Caitlin Zacharias for her help with proofreading this work for grammatical errors.

Table of Contents

Abstract I

Acknowledgments II

List of Tables VI

List of Figures VII

List of Abbreviations and Acronyms IX

1. Introduction 1

2. Background 9

2.1 Ultrasound Imaging 9

2.1.1 Ultrasound Fundamentals 9

2.1.2 Signal Model 12

2.2 Wavelet Theory 14

2.2.1 Wavelet Transforms 14

2.2.2 Wavelet Shrinkage 17

2.2.3 Wavelet Properties 18

2.2.4 WienerChop Denoising 20

2.3 Deconvolution 22

2.3.1 Convolution 22

2.3.2 Inverse Filters and Stability 23

2.3.3 Blind Deconvolution 24

2.3.4 Iterative vs. Non-Iterative Blind Deconvolution 25

2.3.5 Wiener Deconvolution 26

2.3.6 Cepstrum-domain Reflectivity-Pulse Separation 28

2.3.7 Wavelet Shrinkage of the Log-Spectrum 31

2.3.8 Effects of Stationary Pulse Assumption 34

2.3.9 Quasi-stationary Approach: Wavelet Shrinkage of the Log-Gabor-Spectrum 36

3. Proposed Log-Scalogram Shrinkage Technique 39

3.1 Introduction 39

3.2 CWT Coefficients as Representation of Spectra 40

3.3 Wavelet Selection 40

3.4 Range of Scales for CWT 41

3.5 Summary of Method 43

3.6 WienerChop Modification 44

4. Optimized Parameter Selection 46

4.1 Introduction 46

4.2 Heuristic Optimization 47

4.3 Cost Functions 48

5. Experiment 52

6. Results and Discussion 55

6.1 Proposed Technique vs. Log-Spectrum Shrinkage Method 56

6.2 Parameter Optimization 60

6.3 WienerChop Modification 64

6.4 Additional Discussion 68

7. Conclusion 70

References 72

Appendix A: Transducer Datasheets 77

Appendix B: Pulser Datasheets 78

Appendix C: MATLAB Code 86

List of Tables

Table 4.3-1: Parameters Selected with Various Cost Functions 51

Table 6.1-1: Quality Metric Comparison of Methods 60

Table 6.2-1: Quality Metrics for Cost-Optimized Single CWT-Basis Images..... 64

Table 6.3-1: Quality Metrics for Cost-Optimized Dual CWT-Basis Images 68

List of Figures

Figure 1-1: Cross-sectional photo of a power cable with the XLPE labeled 7

Figure 2.1.1-1: Simulated near-field point-spread function 11

Figure 2.3.8-1: Example of ringing effect in Fourier-domain Wiener deconvolution 36

Figure 3.4-1: Example scan (top) and the magnitude of its corresponding CWT-coefficients from scales 1-100 (bottom) 42

Figure 5-1: Cross-sectional photo of power cable (enlarged) 53

Figure 6-1: Unprocessed B-scan image 56

Figure 6.1-1: Results of stationary log-spectrum shrinkage-based deconvolution 57

Figure 6.1-2: Results of quasi-stationary log-spectrum shrinkage-based deconvolution 58

Figure 6.1-3: Results of proposed log-scalogram shrinkage-based deconvolution with empirically selected parameters and a single CWT basis 59

Figure 6.2-1: Results of proposed log-scalogram shrinkage-based deconvolution with entropy-optimized parameters and a single CWT basis 61

Figure 6.2-2: Results of proposed log-scalogram shrinkage-based deconvolution with AW&N-optimized parameters and a single CWT basis 62

Figure 6.2-3: Results of proposed log-scalogram shrinkage-based deconvolution with fractal dimension-optimized parameters and a single CWT basis 63

Figure 6.3-1: Results of proposed log-scalogram shrinkage-based deconvolution with entropy-optimized parameters and dual CWT basis 65

Figure 6.3-2: Results of proposed log-scalogram shrinkage-based deconvolution with AW&N-optimized parameters and dual CWT basis 66

Figure 6.3-3: Results of proposed log-scalogram shrinkage-based deconvolution with fractal dimension-optimized parameters and dual CWT basis 67

List of Abbreviations and Acronyms

AW&N – Autocorrelation width and noise (metric introduced in this work)

AWGN – Additive white Gaussian noise

CWT – Continuous wavelet transform

DC – Direct current

DWT – Discrete wavelet transform

MRI – Magnetic resonance imaging

NDT – Non-destructive test

PSNR – Peak signal-to-noise ratio

XLPE – Cross-linked polyethylene

1. Introduction

Ultrasonic imaging provides a means of internal inspection of structures for applications in which imaging technologies such as MRI, X-ray, et cetera prove too expensive or lack portability. For industrial applications, ultrasonic imaging may serve as a method of quality control, fault detection and analysis, or process control. However, the effective visualization of faults in ultrasonic imaging suffers from noise as well as blurring due to the finite time-duration of the pulse [1]. A new method of blind deconvolution and denoising of ultrasound is presented in this work to reduce the blurring effect caused by the pulse width and to remove noise from the image. Several modifications to the method are also discussed and their effects on the performance of the method are shown experimentally.

Noise in ultrasound images can be present as multiplicative speckle noise – attributed to random interference of coherent waves scattering within a medium – or system noise, which is typically modeled as additive white Gaussian noise (AWGN) [2]. Several wavelet-based techniques have been developed to denoise signals and are considered herein as the foundation for the methods introduced. In [3] Donoho and Johnstone introduced the concepts of wavelet shrinkage – calculating the wavelet transform of a noisy signal, setting to zero all wavelet transform coefficients below a certain threshold and reconstructing the noise-free estimate by the inverse wavelet transform – as a means of removing AWGN from signals. More specific to ultrasound denoising, [4] and [5] apply wavelet shrinkage to the log-transformed ultrasound image, effectively treating the multiplicative speckle noise as additive noise. A whitening filter

is used in [4] to decorrelate the speckle noise prior to log-transformed wavelet shrinkage, i.e. to make the log-transformed speckle noise more similar to AWGN. Alternatively, in [5] cycle-spinning is included in the Discrete Wavelet Transform (DWT) for shift-invariance to ensure weak details in the image are detected in the presence of noise. The performance of different threshold selection techniques is also discussed in [5].

The foundation for wavelet shrinkage denoising techniques is a sparse representation of the signal in the wavelet domain while comparatively the noise spreads over a wider range of wavelet coefficients. Implementing this for the case of ultrasound denoising the mother wavelet can be selected to resemble the ultrasound pulse. Thus, with proper wavelet selection, wavelet coefficient shrinkage will enhance the desired pulse back-scattering information relative to noise upon reconstruction [6].

In ultrasound imaging a high-frequency acoustic pulse is emitted by a transducer in to the imaged structure and its backscattering is recorded as a time-domain signal. The received signal in an ultrasonic pulse-echo imaging system is commonly considered as the convolution of the acoustic reflectivity function of the imaged structure with the point-spread function of the imaging system [7], [1]. Such a signal model resembles that considered for image blur modeling and thus, the point-spread function can be considered as a blurring kernel acting upon the desired material reflectivity function. In a one-dimensional sense, each received ultrasound signal can be considered as an integration of the material reflectivity function over the beam-width of the transducer convolved with the ultrasound pulse. Note that in this case the ultrasound pulse refers not to the pulse emitted in to the imaged medium but rather the emitted pulse convolved with the electromechanical reception transfer function of the transducer. Thus, the longer the

pulse time-duration, the greater the temporal blurring effect. The time-duration of the pulse in ultrasound imaging systems is particularly important in non-destructive test (NDT) applications where multilayer materials are imaged, as the change in acoustic impedance at layer-to-layer interfaces causes reflections that can obscure faults near the interface. This blurring effect is typically reduced by deconvolution of the pulse from the acquired data, as in [1] and [8], which is also the approach taken in this work to enhance the ultrasound scans.

The task of deconvolving the pulse from the received ultrasound echo data necessitates first estimating the pulse. In [9], Jensen and Leeman proposed a non-parametric technique for ultrasound pulse estimation based on the general premise that the pulse magnitude-spectrum was smooth relative to the jaggedness of the material reflectivity function magnitude-spectrum. By taking the aforementioned pulse-reflectivity convolution model to the real cepstrum domain – i.e. the Fourier transform of the log-transformed magnitude of the Fourier spectrum – they surmised that the two functions mostly occupied separate bands in the cepstrum domain and thus were separable. Furthermore, Jensen and Leeman proved experimentally that the pulse spectrum exhibited minimum-phase characteristics for most piezoelectric transducers, which allowed for recovery of the pulse phase-spectrum via the Hilbert transform of the log-magnitude-spectrum.

However, as Adam and Michailovich discussed in [1], the pulse and reflectivity function are not easily separable in the cepstrum domain as there often exists overlap of their components. Working again with the premise that the pulse spectrum was smooth relative to the reflectivity function spectrum, Adam and Michailovich proposed DWT

shrinkage of the received signals log-spectrum to estimate the pulse log-spectrum and again utilized the minimum-phase assumption to recover the complex pulse spectrum via the Hilbert transform. The basis for applying DWT shrinkage to the signal log-spectrum is an interesting property of the wavelet transform: as shown by Daubechies, as cited in [1], the wavelet decomposition of a polynomial results in detail coefficients of zero when the number of vanishing moments of the mother wavelet is greater than the degree of the polynomial. Thus, the smoothness of the pulse log-spectrum was estimated, at least locally, as a polynomial of limited degree and could be reconstructed from the DWT approximation coefficients alone, effectively setting all detail coefficients to zero as a simplified means of wavelet shrinkage. Fourier-domain Wiener deconvolution was then used to deconvolve the estimated pulse from the ultrasound scan data.

The shortcomings of the method proposed by Adam and Michailovich are a result of representing the ultrasound signal spectra in the Fourier domain. More specifically, the Fourier-domain spectral representations are not localized with respect to time due to the Fourier basis not being compact. In the work of Adam and Michailovich, the Fourier-domain analysis implies an assumption of stationarity to the received ultrasound echo, pulse and material reflectivity spectra. However, the pulse in particular may not be stationary due to frequency-dependent attenuation and diffraction effects, which may lead to an inaccurate estimation of the pulse [1]. Fourier-domain Wiener deconvolution also leads to the widely documented issue of Gibbs-phenomena-like ringing effects around sharp edges or transitions in an image or signal [10].

This work proposes a novel technique for deconvolution and denoising of ultrasound for NDT applications. The localization of the signal spectra with respect to

time is addressed in the proposed method. The method by Adam and Michailovich is modified such that the time-localized signal spectra are represented as the multiscale Continuous Wavelet Transform (CWT) coefficients, also referred to as the scalogram herein. The method can be summarized as follows: The CWT scalogram is calculated on the received ultrasound scans; DWT shrinkage is applied to the signals log-transformed CWT scalogram to estimate the pulse log-scalogram; the complex pulse scalogram – i.e. the phase information – is recovered via the Hilbert transform; finally, the Wiener deconvolution occurs in the CWT-domain and the inverse CWT recovers the approximated reflectivity function.

Based on the compaction property of wavelet denoising, as discussed above, the CWT mother wavelet is selected intuitively to resemble the ultrasound pulse by visual inspection. Thus, the scalogram provides a sparse representation of the ultrasound backscattering information relative to the noise. The CWT scales to be considered in the method can be found by analyzing the dominant back-scattering components in the received data or found by optimizing the parameters of the algorithm with respect to a particular quality metric on a training set of the data. The setting of the algorithm parameters, including the CWT scales or pseudo-frequency range, is considered later both by empirical setting and by heuristic optimization.

The resulting algorithm, simply summarized as the method of Adam and Michailovich performed in the CWT-domain, also has the interesting implication that Fourier-domain Wiener filtering is replaced by CWT-domain Wiener filtering as previously mentioned. The concept of wavelet-domain Wiener filtering was first explored by Ghael et al in [11] and was further analyzed in [12]. The method was

dubbed “WienerChop” by analogy to Donoho and Johnstone’s “WaveChop” method [12].

In addition to implementing the Wiener filter in the wavelet domain, the WienerChop method proposes using different basis wavelets for the estimation and deconvolution stages of the algorithm. The motivation for using a second wavelet domain for deconvolution is to reduce the effects of estimation error. By once again taking advantage of the sparse representation of the signal provided by the wavelet transform, the second wavelet basis will spread the estimation error over a large number of coefficients relative to the desired signal information. Incorporating a second CWT basis to the proposed technique based on the principles presented in the WienerChop method is discussed further in this work and its effect on the performance of the proposed methods is determined experimentally.

Although the methods presented in this work apply generally to preprocessing ultrasound NDT, the examples and discussion herein are confined to imaging the cross-linked polyethylene (XLPE) insulation layer of underground power cables. A photograph of a cross-section of an underground power cable is shown in Figure 1-1 with the XLPE layer labeled.

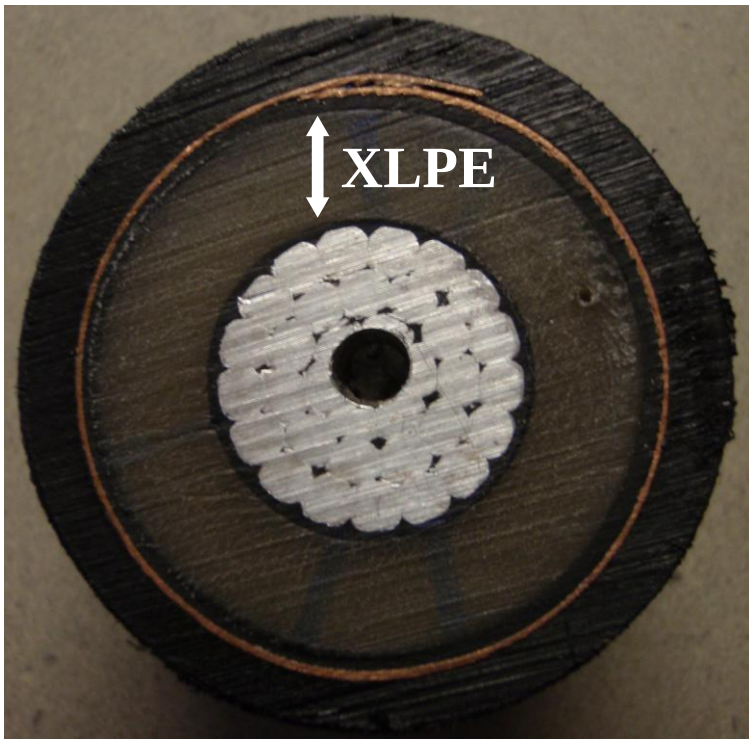

Figure 1-1: Cross-sectional photo of a power cable with the XLPE labeled

One of the major causes of interruption of underground power distribution is dielectric breakdown of the XLPE insulation due to water-trees [13]. Researched here in co-operation with Manitoba Hydro, ultrasonic inspection of XLPE insulation holds real potential for the power distribution industry. Currently XLPE insulation is assessed using a destructive dissection as detailed in [13]. The deconvolution and deblurring methods proposed in this work can be considered as a preprocessing step in the detection and imaging of water-treeing in underground power cables. In the results, Section 6, two-dimensional cross-sectional ultrasound images of a cable are shown before and after processing with the methods discussed.

The effectiveness of the proposed methods with respect to the task of preprocessing ultrasound scans of the power cables by denoising and deblurring is quantified with a variety of performance metrics. An established quality metric such as image entropy is used in conjunction with less common blur metrics discussed in this work: fractal dimension and autocorrelation 6-dB width divided by peak signal-to-noise ratio (PSNR). The proposed technique improved on its predecessors in both visual subjective quality and with respect to the various metrics.

The layout of this work is as follows:

- Section 2 provides general background information including some fundamentals of ultrasound imaging, wavelet denoising (including defining the continuous and discrete wavelet transforms) and existing techniques for deconvolution;
- Section 3 details the proposed deconvolution technique;
- Section 4 discusses parameter optimization for the proposed technique including the various cost functions considered;
- Section 5 reviews the experiment;
- Section 6 contains the results and discussion;
- Section 7 is the conclusion.

2. Background

2.1 Ultrasound Imaging

2.1.1 Ultrasound Fundamentals

Ultrasound imaging is the emission of high-frequency acoustic waves in to a medium and reconstruction of the received echoes over an aperture to form an image. A piezoelectric ultrasound transducer is a piston-like device with a thin membrane driven by an oscillating piezoelectric crystal. The method of ultrasonic imaging considered in this work is with a single piezoelectric transducer in a pulse-echo setup. In the case of imaging underground power cables, the transducer is rotated around the cable circumference for two-dimensional cross-sectional images and along its length for subsequent images. Of course, this imaging methodology requires uncovering a section of the cable from the ground but does not require its removal from service and destruction, as with current methods for XLPE inspection [13].

No focussing techniques are considered in this work. However, it is worth noting that the methods discussed for pre-processing of the ultrasound scans preserve phase information. Thus, the proposed deconvolution method does not preclude the application of techniques such as synthetic aperture focusing based on wave-front reconstruction, as applied in [13] to XLPE imaging. As such, in this case the cross-range resolution, Δy, is dependent on the acoustic beam-width of the transducer, the spread of acoustic energy inside the cable due to refraction and beam-spread, as well as the cross-range sampling rate [13]. The resolution in the range direction, Δx, is given as

$$\Delta x = v/(2\beta) \quad (1)$$

where v is the velocity of sound propagation in the medium and β is the frequency bandwidth of the pulse [14]. To maintain attention in this work on the tasks of deconvolution and denoising, both the time and angular domains will be oversampled – their resolutions and minimum sampling rates will not be considered further.

Another important consideration in ultrasonic imaging is whether the imaging takes place in the near-field or far-field of the transducer. The near-field, as its name implies, refers to the emitted acoustic field closer to the transducer. Since the transducer is not a perfect point-source but rather the acoustic pressure field is generated by movement of the entire surface of the transducer face, it can be considered a collection of point-sources. Furthermore, pressure is not evenly distributed across the transducer face nor is the transducer face entirely free of deflection under its movement so the amplitude and phase of the acoustic field varies along the transducer face. As such, the emitted field immediately in front of the transducer exhibits large fluctuations in amplitude and temporal distortion due to the constructive and destructive interference of the multiple waves. Hereafter, these effects will be referred to simply as the near-field diffraction effects.

Near-field imaging presents challenges in the sense that the temporal distortion of the pulse may make faults show up repeatedly due to temporal distortion, or not at all if the waves interfere destructively at that location. In general, the point-spread function of an ultrasound imaging system – i.e. the appearance of a point-source imaged by the system – is highly non-stationary in the near-field. As an example, Fig. 2.1.1-1 displays a near-field point-spread function created using the Field II ultrasound simulation software

[15], [16]. The plot is shown such that the transducer is at the left of the image facing right – the discrete-time index increases along the horizontal axis to the right and the vertical axis represents the cross-range. The simulation is for a 20mm-diameter 15MHz transducer scanning a point 20mm away in the range direction with a sampling rate of 150MHz. Note that the far-field point-spread function is roughly a hyperbola. In comparison, the near-field point-spread function, as highlighted by Fig. 2.1.1-1, exhibits a much more hectic pattern: when the transducer is axially aligned with the point scatterer, i.e. the point-scatterer is centered on the transducer line-of-sight, three prominent reflections occur.

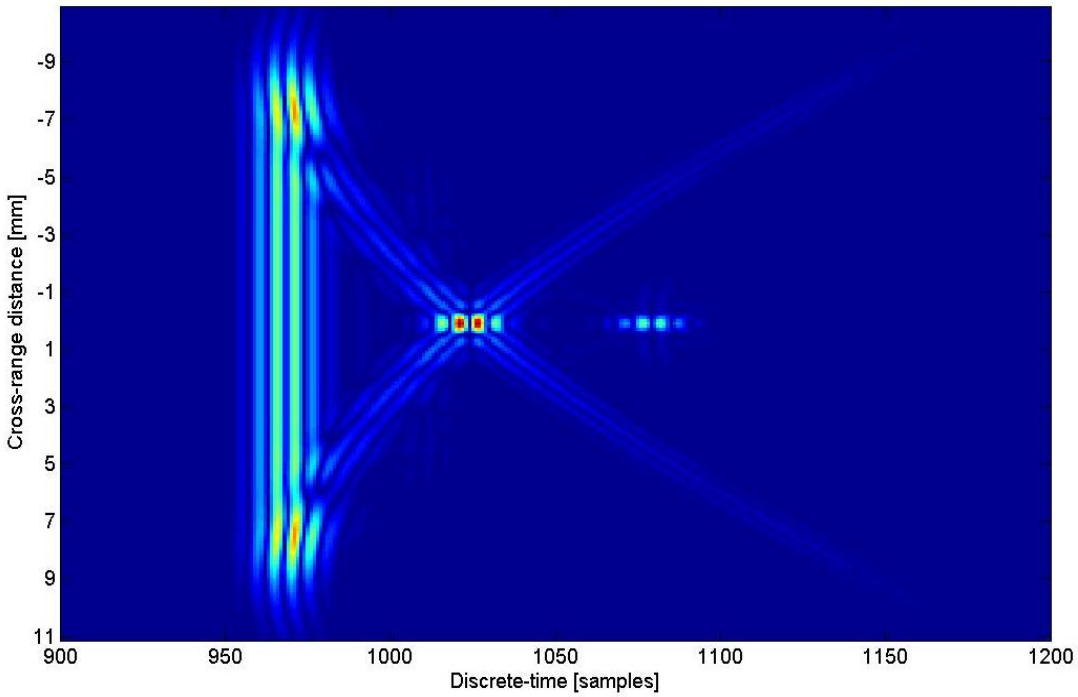

Figure 2.1.1-1: Simulated near-field point-spread function

Conversely, the far-field occurs further away from the transducer where the acoustic field can be approximated as spherical plane waves emanating from a point-

source and which exhibit none of the diffraction effects found in the near-field. The distance from the transducer face to the end of the near-field or the start of the far-field is given as:

$$N = \frac{r^2 f_0}{v} \tag{2}$$

where r is the radius of the transducer, f_0 is the resonant frequency of the piezoelectric transducer and v is the velocity of sound propagation in the medium.

Noise in ultrasound images is generally classified as the following two types: multiplicative speckle noise and AWGN system noise. Multiplicative speckle noise is due to the random constructive and destructive interference of coherent waves scattering within the imaged medium and is responsible for giving ultrasound images their characteristic grainy appearance [2]. System noise, considered as AWGN – modelled as having constant power spectrum density and a Gaussian amplitude distribution – is that induced in the cables by background electromagnetic radiation.

2.1.2 Signal Model

The signal obtained for each scan in a pulse-echo ultrasound imaging system is a time-domain recording of the back-scattering of the emitted pulse convolved with the electromechanical reception response of the transducer. Each scan contains information of scatterers within "view" of the transducer, considering both the beam-spread of the emitted acoustic field and the dimensions of the transducer face. The received pulse-echo ultrasound signal in this work is modeled as a convolution of the point-spread function of the imaging system with the material reflectivity function. The point-spread function of an imaging system represents the appearance of a point-source in the imaged medium

and generally varies with range-distance from the transducer. Ideally, the point-spread function resembles an impulse and the acquired image is simply the desired reflectivity function. A simplified view of this work is that deconvolving the ultrasound pulse reduces the point-spread function support in the range-domain. Similarly, focussing techniques, which are outside the scope considered here as previously mentioned, are generally responsible for reducing the point-spread function cross-range support.

Ignoring acoustic beam-spread in the out-of-plane direction for a two-dimensional image, as well as noise and multiple reflections, the received signal, $s(x, y_n)$, for the transducer at cross-range position index *n*, is given as:

$$s(x, y_n) = p(x, y - y_n) * r(x, y) \tag{3}$$

where p is the point-spread function at distance x from the transducer and r is the material reflectivity function. Equation (2) resembles a model of image blur and thus the point-spread function can be considered as a blurring kernel acting on the material reflectivity function.

Examining a single scan-line in the image, without loss of generality, the discrete-time signal can equivalently be modelled as:

$$s(t) = g(t) * h(t) \tag{4}$$

where $g(t)$ is the ultrasound pulse and $h(t)$ is the one-dimensional result of surface integration over the three-dimensional material reflectivity function at each time instance accounting for beam-spread, refraction and multiple reflections inside the imaged structure. The pulse in (3) can be considered as blurring the reflectivity function or, considering that the ultrasound pulse typically resembles an amplitude modulated sinusoid with multiple peaks, (3) can be interpreted as a repetition of the image edges.

Note that in the case of the signal models presented in (2) and (3), noise has not been considered for sake of introducing the deconvolution problem.

Representing the signal model (3) in the frequency domain, the convolution function becomes multiplication:

$$S(f) = G(f)H(f). \tag{5}$$

The model in (4) can also be represented in its homomorphic form, which serves as the basis for the work in [1], given as:

$$\log\big(S(f)\big) = \log\big(G(f)\big) + \log\big(H(f)\big). \tag{6}$$

2.2 Wavelet Theory

2.2.1 Wavelet Transforms

The wavelet transform, generally speaking, is the decomposition or projection of any arbitrary finite-energy signal by a wavelet basis function and can be considered as a time-frequency representation of the signal. Just as with the well-known Fourier transform (and many other transforms), the wavelet transform represents a signal by its projection on to a basis function – i.e. the projection can be considered a measure of similarity between the signal and the transform basis as performed by the inner product. While the Fourier transform projects a signal on to an orthonormal basis of sine waves over a range of frequencies, the wavelet transform projects the signal on to a set of basis functions generated by a mother wavelet. The mother wavelet, typically with finite time-domain support, is shifted and scaled with respect to time in order to represent time-localized and frequency-localized information, respectively.

In contrast to Fourier-domain analysis of signals, wavelets can be localized with respect to time and are thus better suited to representing signals with piecewise smooth behaviour, large discontinuities, and/or transients – in other words, non-stationary behaviour. Further advantage is provided over even the fixed window length of the Short-Time Fourier transform and Gabor transform due to the scaling of the wavelet support, essentially allowing the wavelet transform to capture broad low-frequency characteristics of the signal while zooming in on high-frequency localized features. As Graps puts it in [17], "*The result in wavelet analysis is to see both the forest and the trees, so to speak*." Of course, the uncertainty principle – that a signal cannot be localized in both time and frequency to an arbitrarily small measure – still applies. However, applying the wavelet transform over multiple scales allows for a multi-resolution analysis as the time and frequency resolutions vary with the wavelet scale. For the sake of thorough introduction to this topic both the CWT and DWT are defined here as follows.

The CWT refers to the use of continuously variable scales and translations of the mother wavelet in the wavelet transform in contrast with the DWT for which these variables can take only a discrete set of values. Although the processing of ultrasound signals considered in this work is strictly confined to discrete-time analysis, for simplicity the CWT will be introduced as applying to continuous-time signals as follows. For an arbitrary continuous-time signal $x(t)$ the CWT coefficients at scale $a > 0$ with the mother wavelet $\psi(t)$ are given as:

$$c_x(\tau, a) = \frac{1}{\sqrt{a}} \int x(t) \psi^* \left(\frac{t-\tau}{a} \right) dt \tag{7}$$

where * denotes the complex conjugate. Alternatively, the translated, normalized and

scaled version of the mother wavelet, $\frac{1}{\sqrt{a}}\psi\left(\frac{t-\tau}{a}\right)$, can be referred to as $\psi_{\tau,a}(t)$ and it becomes readily apparent that (7) is a calculation of the inner product between the given signal and the wavelet transform basis functions:

$$c_x(\tau, a) = \langle x(t), \psi_{\tau,a}(t) \rangle \tag{8}$$

where $\langle ... \rangle$ denotes the inner product. Also note that for any fixed a, $\psi_{\tau,a}$ forms an orthonormal set. The wavelet scaling coefficient a is analogous to the frequency (though inversely proportional) and a time-frequency representation of a signal can be given as the CWT coefficients calculated over a range of scales.

The DWT represents a signal in terms of its approximation and detail coefficients, as found by the inner product of the signal with the scaling wavelet $\varphi(t)$ and analysis wavelet $\psi(t)$, respectively. As their names suggest, the approximation and detail coefficients contain information on the signals broad shape-defining features and small localized details, respectively. In the dyadic DWT, the algorithm used in this work, the approximation and detail coefficients are down-sampled or decimated by a factor of two at each decomposition level. For example, the first decomposition of a signal with *N* samples contains roughly *N*/2 approximation coefficients and *N*/2 detail coefficients. Each subsequent decomposition of the signal to a larger scale applies then to the decimated approximation coefficients of the previous level rather than the original signal. The signal is still completely described by its down-sampled approximation and detail coefficients provided ψ and φ span orthogonal complements of each other. Note however, that the decimation causes the DWT to not be shift invariant. To attain shift invariance of the DWT, cycle-spinning can be employed as in [18]: the shift variance is

cancelled by applying the DWT to shifted copies of the original signal then un-shifting and averaging.

2.2.2 Wavelet Shrinkage

Wavelet shrinkage for denoising entails applying a wavelet transform, CWT, DWT or other, to a noisy signal, shrinking to zero all coefficients below a certain threshold, and then reconstructing an estimate of the noise-free signal via the inverse wavelet transform. Wavelet shrinkage was first introduced by Donoho and Johnstone in [3]. Ever since, wavelet denoising has grown increasingly popular, with a variety of techniques proposed on threshold selection methods and a wide range of applications studied.

As mentioned earlier, the wavelet transform is suited to represent both broad shape-defining characteristics and localized high-frequency details of a signal due to the scaling of the wavelet support, which allows for multi-resolution analysis. Furthermore, when the mother wavelet resembles either desired or prominent features of the signal, such as edges in image analysis or the pulse in ultrasound processing, multi-resolution analysis of the wavelet transform results in a sparse representation of the signal in an over-complete dictionary of basis functions. That is, the prominent or desired information of the signal is represented compactly in a few coefficients relative to the total number of coefficients available. Considering the wavelet transform defined by the inner product in (8), which provides a measure of similarity between the scaled wavelet and the signal, it becomes clear how a wavelet resembling certain characteristics of the signal would provide a compact representation of those characteristics. Conversely, the noise content of the signal will be spread out over a wider range of scales comparatively.

Thus, when all wavelet coefficients below a certain threshold are shrunk to zero and the signal is reconstructed via the inverse wavelet transform it is possible to reduce noise without affecting some characteristics of the signal, for example the edges.

Thresholding can be implemented in two ways: hard thresholding, in which all wavelet coefficients of absolute value less than the threshold are set to zero and larger coefficients are left unchanged; or soft thresholding, in which all wavelet coefficients of absolute value less than the threshold are set to zero and larger coefficients are reduced by the threshold value. For clarity, the two methods of thresholding a sequence of wavelet coefficients $c(\tau)$ are given as:

$$\text{Hard Thresholding: } \hat{c}(\tau) = \begin{cases} c(\tau), & |c(\tau)| > \gamma \\ 0, & |c(\tau)| \leq \gamma \end{cases} \tag{9}$$

$$\text{Soft Thresholding: } \hat{c}(\tau) = \begin{cases} c(\tau) - \gamma, & |c(\tau)| > \gamma \; and \; c(\tau) > 0 \\ c(\tau) + \gamma, & |c(\tau)| > \gamma \; and \; c(\tau) < 0 \\ 0, & |c(\tau)| \leq \gamma \end{cases} \tag{10}$$

where γ is the threshold being applied, which in general is a function of the coefficients. Since the methods of ultrasound deconvolution and denoising discussed in this work are only related to wavelet shrinkage and don't require a threshold to be selected, the many methods of threshold setting are not discussed here.

2.2.3 Wavelet Properties

The set of translated wavelets at a fixed scale must be linearly independent and span the signal space – i.e. the wavelets must form a basis for the signal such that the signal has a unique representation as its wavelet coefficients [19]. A wavelet $\psi(t)$ is also required to satisfy the admissibility condition, which is given as:

$$\int \frac{|\Psi(\omega)|^2}{|\omega|} d\omega < \infty \tag{11}$$

where $\Psi(\omega)$ is the Fourier transform of $\psi(t)$. The admissibility condition in (11) also implies that

$$\Psi(0) = \int \psi(t)\, dt = 0. \tag{12}$$

That is, the wavelet has no DC offset. All wavelets used or discussed in this work will be traditional (with respect to the relatively new field of wavelets) and as such their definition and proof of admissibility will be omitted.

Another property of the wavelet to consider is its number of vanishing moments or order. For a wavelet with K vanishing moments, the wavelet transform can provide an error-free representation of polynomials of order less than K – as mentioned previously, the pulse estimation techniques in this work rely on this property to produce null detail coefficients for a polynomial of order less than the wavelet vanishing moments. The number of vanishing moments K for a wavelet ψ is defined in the Fourier domain as:

$$\Psi^{(k)}(0) = 0 \text{ for } k = 0, \dots, K-1 \tag{13}$$

where $\Psi^{(k)}(0)$ denotes the k^{th} derivative with respect to ω at $\omega = 0$ [19]. Alternatively, the vanishing moments may be defined in the time domain, as in agreement with the typical definition of a moment, as:

$$\int t^k \psi(t)\, dt = 0 \text{ for } k = 0, \dots, K-1. \tag{14}$$

Note that (14) for $k = 0$ reduces to (12), an implication of the admissibility condition. As such, all wavelets have at least one vanishing moment. An example of a wavelet with only one vanishing moment is the Haar wavelet.

Although wavelets within a given family – ex. Daubechies, Coiflets, Symlets, etc. – generally appear smoother as the number of vanishing moments increases, the number of vanishing moments does not directly imply smoothness as defined by the order of continuous derivatives with respect to time. That is, a wavelet with K vanishing moments does not necessarily have K continuous derivatives. This can be shown by the example of the Haar wavelet, which by (12) and (14) has one vanishing moment but has a discontinuous first derivative. The opposite does apply, however – a wavelet with K continuous derivatives with respect to time will have at least K vanishing moments.

Another property of wavelets considered in this work is the compactness of the mother wavelet. The compactness of a wavelet considered in analysis of time-domain signals can be described simply as having a finite time-duration. More specifically, the wavelet has bounded support and vanishes at infinity, i.e. $\psi(t) \to 0$ as $t \to \pm\infty$. An example of a non-compact wavelet is the Shannon wavelet. For the purposes of this work only compact mother wavelets will be used.

2.2.4 WienerChop Denoising

The WienerChop method of denoising was first introduced by Ghael, Sayeed and Baraniuk in [11] and was later further analyzed by Choi and Baraniuk in [12]. Once again, the motivation is to remove AWGN from signals. The WienerChop method proposes applying Wiener filtering to individual wavelet coefficients – i.e. Wiener filtering in the wavelet domain rather than the Fourier domain – to reduce noise. As with Fourier-domain Wiener filtering, the challenge is designing the Wiener filter without first knowing the noise-free signal.

In order to design the wavelet-domain Wiener filter, the WienerChop method proposes using wavelet shrinkage with hard thresholding to estimate the noise-free signal. Essentially, the WienerChop method employs traditional wavelet thresholding and shrinkage, itself a denoising technique, as a preliminary estimate to design the Wiener filter. As was shown in [11], the WienerChop method outperforms the use of wavelet thresholding and shrinkage alone.

Besides implementing the well-known Wiener filter in the wavelet domain rather than the Fourier domain, another interesting aspect of the WienerChop method is its use of two wavelet domains. More specifically, the estimation of the noise-free signal to design the Wiener filter occurs in a separate wavelet domain from the implementation of the Wiener filter. The motivation for this is due to the sparse representation of the signal provided by the wavelet transform, just as it was for wavelet shrinkage. That is, the Wiener filter is implemented in an alternate wavelet domain such that the estimated noise-free signal information is represented by few wavelet coefficients relative to the estimation error. Thus, the effects of error in the estimation stage on the final result are reduced.

The performance of the WienerChop method with respect to the wavelet basis selections is difficult to formulate, as noted in [12]. Since both the estimation and deconvolution wavelet domains require a compact representation of the signal both wavelets must be suited to the signal. However, the wavelets must also be sufficiently different such as to spread the estimation error from the first domain over a wide range of coefficients in the second.

For a noisy signal modeled as $s(t) = x(t) + n(t)$, where $x(t)$ is the true noise-free signal and $n(t)$ is AWGN, the objective is to approximate $x(t)$ in a minimum mean-square error sense. The WienerChop method can be summarized as follows:

1. The noisy signal is taken to the first wavelet domain, denoted here as W_1 for clarity; $s(t) \leftrightarrow c_{s,1}(\tau)$.
2. The signal is first denoised by wavelet shrinkage with hard thresholding; $c_{s,1}(\tau) \rightarrow \hat{c}_{x,1}(\tau)$.
3. The estimated noise-free signal is then reconstructed via inverse wavelet transform; $\hat{c}_{x,1}(\tau) \leftrightarrow \hat{x}(t)$.
4. Both the original noisy signal and its noise-free estimate are transformed to the second wavelet domain, W_2; $s(t) \leftrightarrow c_{s,2}(\tau)$, $\hat{x}(t) \leftrightarrow \hat{c}_{x,2}(\tau)$.
5. Wiener filtering is then implemented in the second wavelet domain and applied to the signal coefficients as: $\tilde{c}_{x,2}(\tau) = c_{s,2}(\tau) \frac{\hat{c}_{x,2}^2(\tau)}{\hat{c}_{x,2}^2(\tau)+\sigma^2}$, where σ^2 is the variance of the noise.
6. The final approximation of the noise-free signal is recovered via the inverse wavelet transform; $\tilde{c}_{x,2}(\tau) \leftrightarrow \tilde{x}(t)$

2.3 Deconvolution

2.3.1 Convolution

Convolution is typically used to model the behaviour of linear time-invariant systems with respect to the systems impulse response and a given input signal. More

specifically, a system with impulse response $h(t)$ excited by an input signal $x(t)$ will produce an output given by the convolution of $h(t)$ with $x(t)$, denoted $h(t) * x(t)$, defined in continuous-time as:

$$h(t) * x(t) = \int_{-\infty}^{\infty} h(\tau)x(t-\tau)\,d\tau \tag{15}$$

The equivalent representation in the frequency domain is given by the product of the two functions:

$$h(t) * x(t) \leftrightarrow H(f)X(f) \tag{16}$$

2.3.2 Inverse Filters and Stability

The representation in (16) is important in considering the task of deconvolving $h(t)$ from the resulting signal. On first appearance, (16) would indicate that removing the effects of convolution with the system impulse function $h(t)$ would be as simple as implementing an inverse filter – i.e. dividing by $H(f)$ in the frequency domain. However, notice that if $H(f)$ equals zero, the inverse-filter would be unstable. To further assess the stability of the inverse filter, one may consider whether the system is minimum-phase or not.

A minimum-phase system is defined as having a net change of zero over its phase spectrum [20]. In other words, speaking in terms of normalized radian frequency – ranging from zero to pi – the phase of the system frequency response is equal at frequencies of zero and pi. In terms of the complex *S*-plane, this implies all the zeros of the system are on the left half-plane. Equivalently, this means all the zeros of the system are inside the unit circle on the complex *Z*-plane. The implications on the stability of the inverse filter are as follows:

- The inverse of a minimum-phase system is stable due its poles being entirely on the left half *S*-plane.
- A minimum-phase system that is stable – i.e. all of its zeros and poles are on the left half S-plane – has an inverse that is also stable and minimum-phase.

The stability of the inverse filter can be improved for a non-minimum-phase system by adding a constant to the magnitude of the system frequency response. This technique is referred to as regularization in this context and is discussed further in section 2.3.5 in the framework of the Wiener filter.

2.3.3 Blind Deconvolution

Blind deconvolution refers to deconvolution without an initial estimate of the response of the system to be deconvolved. In other words, blind deconvolution estimates the system response based on the data from which it is to be deconvolved. In the context of ultrasound deconvolution the system response to be deconvolved is the ultrasound pulse.

Existing non-blind deconvolution techniques for ultrasound approximate the pulse prior to scanning. This can be achieved by system characterization as in [21] – where the transfer functions of the transducer, pulser and connecting cables are determined experimentally – or by recording the reflection from a single scatterer such as a thin wire phantom as in [22]. The limitation of these techniques is that they fail to account for the pulse varying over the length of the received signals. More specifically, these non-blind techniques neglect to consider diffraction effects if imaging takes place

in the near-field or frequency-dependent attenuation in the imaged structure. Since the imaging in this work takes place in the near-field of the transducer where the point-spread function is highly non-stationary, blind deconvolution techniques are more suitable for this application and non-blind techniques are not considered further.

2.3.4 Iterative vs. Non-Iterative Blind Deconvolution

Blind deconvolution can be performed either iteratively or non-iteratively. Iterative blind deconvolution techniques aim to progressively improve the estimation of the system response to be deconvolved at each iteration with respect to a certain quality metric applied to the deconvolved image or signal. Conversely, non-iterative techniques make an initial estimate from the data and apply deconvolution only once.

While iterative techniques can be more complex and generally return more accurate estimations of the deconvolved system response, non-iterative blind deconvolution is considered in this work primarily for two reasons:

- The ultrasound pulse to be deconvolved is considered highly non-stationary in the near-field imaging used in this application. Thus, iterative techniques are missing an important constraint on the estimate of the system response.
- The computational requirement of non-iterative techniques is generally less than iterative techniques. This may eventually be a crucial requirement for implementing a field-ready ultrasound imaging system for underground power cables. That is, where processing time is ideally

limited to time between scans and implementation occurs on a portable workstation such as a tablet computer.

2.3.5 Wiener Deconvolution

Wiener deconvolution is commonly used in deconvolution problems in the presence of noise and/or an unstable inverse filter. Referring back to the ultrasound signal model in (4), the same variables can be used again here for simplicity and additive noise can also be considered. That is, $s(t) = g(t) * h(t) + u(t)$ is the available data, $h(t)$ is an unknown input signal to the system $g(t)$, and $u(t)$ is additive noise, which need not be white Gaussian for the purposes of this explanation. Assume also for the sake of explanation that $g(t)$ is either known explicitly or that the effects of estimation error will be neglected in the design of the deconvolution filter. The Wiener deconvolution filter to approximate $h(t)$ can then be derived as follows.

Suppose that for the system defined as $s(t) = g(t) * h(t) + u(t)$ the Wiener deconvolution filter in the time domain, $w(t)$, approximates $h(t)$ as $\tilde{h}(t) = w(t) * s(t)$. The mean-square error can then be defined as:

$$\varepsilon(f) = \mathbb{E}\left\{\left|h(t) - \tilde{h}(t)\right|^2\right\} = \mathbb{E}\left\{\left|H(f) - \widetilde{H}(f)\right|^2\right\} \tag{17}$$

where $\mathbb{E}\{...\}$ is the expectation operator. Substituting for $\widetilde{H}(f)$ as:

$$\varepsilon(f) = \mathbb{E}\{|H(f) - W(f)S(F)|^2\} \tag{18}$$

then substituting again for $S(f)$,

$$\varepsilon(f) = \mathbb{E}\{|H(f) - W(f)[G(f)H(f) + U(f)]|^2\} \tag{19}$$

$$= \mathbb{E}\{|H(f)[1 - W(f)G(f)] - W(f)U(f)|^2\} \tag{20}$$

$$= |1 - W(f)G(f)|^2\mathbb{E}\{|H(f)|^2\}$$

$$-[1 - W(f)G(f)]W^*(f)\mathbb{E}\{H(f)U^*(f)\}$$

$$-[1 - W(f)G(f)]^*W(f)\mathbb{E}\{H^*(f)U(f)\}$$

$$+|W(f)|^2\mathbb{E}\{|U(f)|^2\}. \quad (21)$$

Then if the desired deconvolved signal $h(t)$ is independent of the noise $u(t)$, the expectations in the second and third terms of (21) equal zero.

$$\varepsilon(f) = |1 - W(f)G(f)|^2\mathbb{E}\{|H(f)|^2\} + |W(f)|^2\mathbb{E}\{|U(f)|^2\} \quad (22)$$

$$= [1 - W(f)G(f)][1 - W^*(f)G^*(f)]\mathbb{E}\{|H(f)|^2\} + W(f)W^*(f)\mathbb{E}\{|U(f)|^2\} \quad (23)$$

In order to find the minimum mean-square error with respect to the Wiener filter, take the derivative of $\varepsilon(f)$ with respect to $W(f)$ and set it equal to zero:

$$\frac{\partial\varepsilon(f)}{\partial W(f)} = -G(f)[1 - W^*(f)G^*(f)]\mathbb{E}\{|H(f)|^2\} + W^*(f)\mathbb{E}\{|U(f)|^2\} = 0 \quad (24)$$

Rearranging and conjugating to solve for $W(f)$:

$$W(f) = \frac{G^*(f)}{|G(f)|^2 + \mathbb{E}\{|U(f)|^2\}/\mathbb{E}\{|H(f)|^2\}} = \frac{G^*(f)}{|G(f)|^2 + 1/SNR(f)}. \quad (25)$$

Notice that if the signal-to-noise ratio is infinite, the Wiener deconvolution filter reduces to the simple inverse filter. Otherwise, the second term of the denominator can be considered as a regularization of the ill-posed division. Often the regularization term is simplified as a constant due to lack of knowledge of the input signal spectrum, the noise spectrum, or both. It is also worth noting that, as shown in the derivation, the Wiener deconvolution filter is optimal in the minimum mean-square error sense with respect to the estimate of the system $g(t)$.

2.3.6 Cepstrum-domain Reflectivity-Pulse Separation

A blind deconvolution technique for ultrasound may be designed around some assumptions of the pulse in order to facilitate its estimation from the acquired data and subsequently its deconvolution. For instance, Jensen and Leeman introduced a novel method for non-parametric pulse estimation and blind deconvolution in [9]. The pulse estimation relied on the general assumption that the pulse magnitude-spectrum was smooth relative to the jagged reflectivity function magnitude-spectrum. Jensen and Leeman note:

"*The spectrum of the pulse is smooth and band limited. This is to be expected as a transducer is an electromechanical resonant device that can be described well by a relatively simple model with a few degrees of freedom. The tissue reflection sequence is a complex signal with numerous spikes and dips due to the complex underlying structure of the tissue.*"

By avoiding a parametric model of the pulse, as Jensen and Leeman mention, the pulse estimate is less confined to the model being used.

Recalling the signal model presented in (4) – that is, the received signal $s(t)$ represented as a convolution of the pulse $g(t)$ and the equivalent one-dimensional material reflectivity function $h(t)$ – the log-magnitude spectrum is given as:

$$s(t) = g(t) * h(t) \rightarrow \log|S(f)| = \log|G(f)| + \log|H(f)|. \quad (26)$$

Under the aforementioned assumption that the pulse magnitude-spectrum is smooth relative to the material reflectivity magnitude-spectrum, the representation in (26) can be considered as the superposition of a smooth slowly-varying function with a jagged rapidly-varying function. Applying the Fourier transform, denoted here as $\mathcal{F}(\dots)$, once

more, (26) becomes:

$$\mathcal{F}(\log|S(f)|) = \mathcal{F}(\log|G(f)|) + \mathcal{F}(\log|H(f)|) \tag{27}$$

which is the real cepstrum-domain representation of (4). Note that for the complex cepstrum-domain representation of (4) the complex-spectra are used rather than the magnitude-spectra.

Thus, if the pulse magnitude-spectrum is smooth relative to the material reflectivity function magnitude-spectrum, Jensen and Leeman propose that the two functions mostly occupy distinct sub-bands in the cepstrum-domain. In order to separate the pulse and the material reflectivity function only a cepstrum cut-off, c_0, is required, below which all components of the real cepstrum of the acquired ultrasound scans are attributed to the estimated pulse, $\mathcal{F}(\log|\tilde{G}(f)|)$. More precisely, the real cepstrum of the estimated pulse is given as:

$$\Re\{C_G(n)\} = \mathcal{F}\left(\log|\tilde{G}(f)|\right) = \begin{cases} \Re\{C_S(n)\} = \mathcal{F}(\log|S(f)|), & |n| < c_0 \\ 0, & |n| \geq c_0 \end{cases} \tag{28}$$

where $\Re\{...\}$ denotes the real-valued set and $C_G(n)$ denotes the cepstrum of $G(f)$.

After estimating the log-magnitude-spectrum of the pulse the next challenge is estimating the phase-spectrum. To accomplish recovery of the phase spectrum from the estimated log-magnitude spectrum, Jensen and Leeman proved experimentally that the pulse exhibits minimum-phase characteristics. Thus, the pulse phase-spectrum is given by the Hilbert transform, denoted here as $\mathcal{H}(...)$, calculated on the estimated pulse log-magnitude-spectrum:

$$\angle\tilde{G}(F) = \mathcal{H}(\log|\tilde{G}(f)|) \tag{29}$$

The shortcomings of the cepstrum-domain pulse estimation proposed by Jensen and Leeman are as follows:

- The pulse is assumed stationary, which makes the technique less suited to near-field imaging or applications with frequency-dependent attenuation.
- There may exist a significant overlap of the pulse and material reflectivity function in the cepstrum-domain such that the pulse estimation accuracy is degraded.

On the first of these limitations, Jensen and Leeman note the non-stationarity of the pulse in the introduction of [9]:

"*Thus, it is commonly assumed that the received pulse-echo signal may be expressed as a depth-dependent pulse convoluted with a tissue reflectivity function. In such models, both the pulse amplitude and shape are dependent on depth in tissue. This results from the frequency-dependent attenuation processes, which lead to the observed nonstationarity of the special properties of the rf line from tissue (as revealed by short-time Fourier analysis, for example).*"

In regards to the second shortcoming, contrary to the premise of the method, there exists sufficient overlap of the pulse and material reflectivity function in the cepstrum domain as to question the validity of implementing a simple cut-off as the means of separation. Assessing the plotted examples in [9] visually, the general premise that the pulse magnitude-spectrum is smooth relative to the material reflectivity function magnitude-spectrum appears to be true. However, there also appears to be significant overlap of the two functions in the cepstrum domain. As such, it seems that the premise

behind the work of Jensen and Leeman is valid but that there may be a better means of separating the functions by this premise. Such an improvement is detailed in the following subsection.

2.3.7 Wavelet Shrinkage of the Log-Spectrum

Taking the work of Jensen and Leeman as the foundation for a new pulse estimation method, in [1] Adam and Michailovich proposed applying wavelet shrinkage to the ultrasound log-magnitude-spectrum. Based on the same premise that the pulse log-magnitude-spectrum is smooth relative to the material reflectivity function log-magnitude-spectrum, Adam and Michailovich surmised that the two functions can be considered as being composed at different scales. Thus, the pulse and material reflectivity function can be separable by wavelet shrinkage of the log-magnitude-spectrum rather than considering their representation in the cepstrum domain.

In [1] Adam and Michailovich considered that the smoothness of the pulse log-magnitude-spectrum can be described, at least locally, as a polynomial of a limited degree. Considering the pulse log-magnitude-spectrum as a polynomial allowed the use of an interesting property of the wavelet transform proven by Daubechies, as cited in [1]: the wavelet decomposition of a polynomial results in detail coefficients of zero when the number of vanishing moments of the mother wavelet is greater than the degree of the polynomial. Alternatively, this can be interpreted as the DWT approximation coefficients providing a complete description of a polynomial when the number of vanishing moments of the mother wavelet exceeds the degree of the polynomial.

In the context of the pulse estimation this property of the wavelet transform implies that DWT decomposition of the received ultrasound data can be used to separate the pulse log-magnitude-spectrum and material reflectivity function log-magnitude-spectrum. Thus, the pulse log-magnitude spectrum can be reconstructed from the approximation coefficients alone. Another interpretation is that the pulse log-magnitude-spectrum is estimated from the acquired ultrasound log-magnitude-spectrum via a simplified implementation of wavelet shrinkage in which all the detail coefficients are set to zero – i.e. the detail coefficients threshold is set to infinity.

Again based on the cepstrum-domain method of Jensen and Leeman, Adam and Michailovich utilized the Hilbert transform of the log-magnitude-spectrum to recover the phase-spectrum using the assumption that the pulse was minimum-phase. To simplify the later comparison, the pulse estimation method of Adam and Michailovich is followed by Wiener deconvolution in this work – the mollifier used to smooth the inverse filter is neglected. The method can be summarized as follows:

1. Calculate the Fourier transform and subsequently the log-magnitude-spectrum of the acquired ultrasound signals;
   $s(n) \rightarrow \log|S(f)| = \log|G(f)| + \log|H(f)|$
2. Apply DWT decomposition to $\log|S(f)|$ using the Symlet wavelet with six vanishing moments to a decomposition level of seven. Note the vanishing moments are in agreement with the range given in [1] and the decomposition level is dependent on sampling rate and recording length, also as stated in [1] – both were found empirically.

3. Reconstruct the pulse log-magnitude-spectrum estimate $\log|\tilde{G}(f)|$ from the DWT approximation coefficients and recover its phase via the Hilbert transform
4. Wiener deconvolution simplified as: $\widetilde{H}(f) = \frac{S(f)\tilde{G}^*(f)}{|\tilde{G}(f)|^2+\varepsilon}$, where ε is a constant proportional to the noise level (as derived in Section 2.3.5); and inverse Fourier transform, $\widetilde{H}(f) \leftrightarrow \tilde{h}(t)$.

Adam and Michailovich note that the mother wavelet should have vanishing moments between four and six – as satisfied by the above specified implementation. Furthermore, they found experimentally that minimum-phase or nearly symmetric mother wavelets yielded the best results. Hence, the Symlet wavelet was used in this work.

The accuracy of this method of pulse estimation depends on the selection of the vanishing moments for the DWT mother wavelet and how it matches the smoothness of the unknown pulse log-magnitude-spectrum. As with the work of Jensen and Leeman, there may exist some overlap of components between the two functions; Hypothetically, even if the pulse log-magnitude-spectrum was completely represented as a polynomial of limited degree and the mother wavelet vanishing moments was chosen to exceed the degree of the polynomial by only one, the material reflectivity function log-magnitude-spectrum may contain smoother components. However, the results in [1] do illustrate the effectiveness of pulse estimation by wavelet shrinkage of the log-magnitude-spectrum. Likewise, the performance of the technique did not vary much with respect to the

selection of the vanishing moments – this is in agreement with the observation of Adam and Michailovich.

Other parameters to be selected for implementation are the DWT decomposition level – related to the frequency resolution and hence dependent on the signal length and sampling rate – and the Wiener deconvolution regularization coefficient ε.

In summary, the pulse estimation method proposed by Adam and Michailovich in [1] improves on work of Jensen and Leeman in [9] with regards to the separation of the pulse and material reflectivity function log-magnitude-spectra. Based again on the premise that the pulse log-magnitude-spectrum was smooth relative to the material reflectivity function log-magnitude-spectrum, the cepstrum-domain cut-off of Jensen and Leeman, essentially an ideal low-pass filtering of the log-magnitude-spectrum, was replaced by DWT shrinkage. However, this improvement did not address the issue of non-stationary behaviour of the pulse, which is discussed in the following subsection.

2.3.8 Effects of Stationary Pulse Assumption

One shortcoming common to both the work of Jensen and Leeman [9] as well as the work of Adam and Michailovich [1] is that the pulse is assumed to be stationary in each method of pulse estimation. The assumption of stationarity in both techniques allows for the use of the Fourier transform to represent the frequency spectra of the analyzed signals. As detailed in Section 2.2.1, the basis function for the Fourier transform is not localized with respect to time and is not well-suited for representing functions with non-stationary characteristics.

As discussed in Section 2.1.1, in near-field ultrasonic imaging the pulse is highly non-stationary due to diffraction effects – in fact, this can be considered the defining feature of the ultrasound near-field in this context. Also, as mentioned by Jensen and Leeman in [9] and quoted above, the pulse "*amplitude and shape*" are depth-dependent due to frequency-dependent attenuation in the imaged material(s). Thus, the pulse cannot be assumed stationary, particularly when imaging takes place in the near-field as it does in this work.

Furthermore, Fourier-domain Wiener deconvolution leads to the well-documented ringing effect around sharp edges or transitions in the image or signal, similar to Gibbs phenomena [10]. To illustrate this effect, Fig. 2.3.8-1 presents an example of a square pulse (top left) being convolved with a Gaussian-windowed sine wave of some arbitrary frequency (top right). The result of convolution with AWGN is shown bottom left for completeness. Wiener deconvolution, as derived in Section 2.3.5, was employed with complete knowledge of the original square pulse signal, the Gaussian-windowed sine wave and the noise. The result (bottom right) shows an overshoot and ringing effect around the sharp transitions of the square pulse signal, as is typically attributed to Gibbs phenomena.

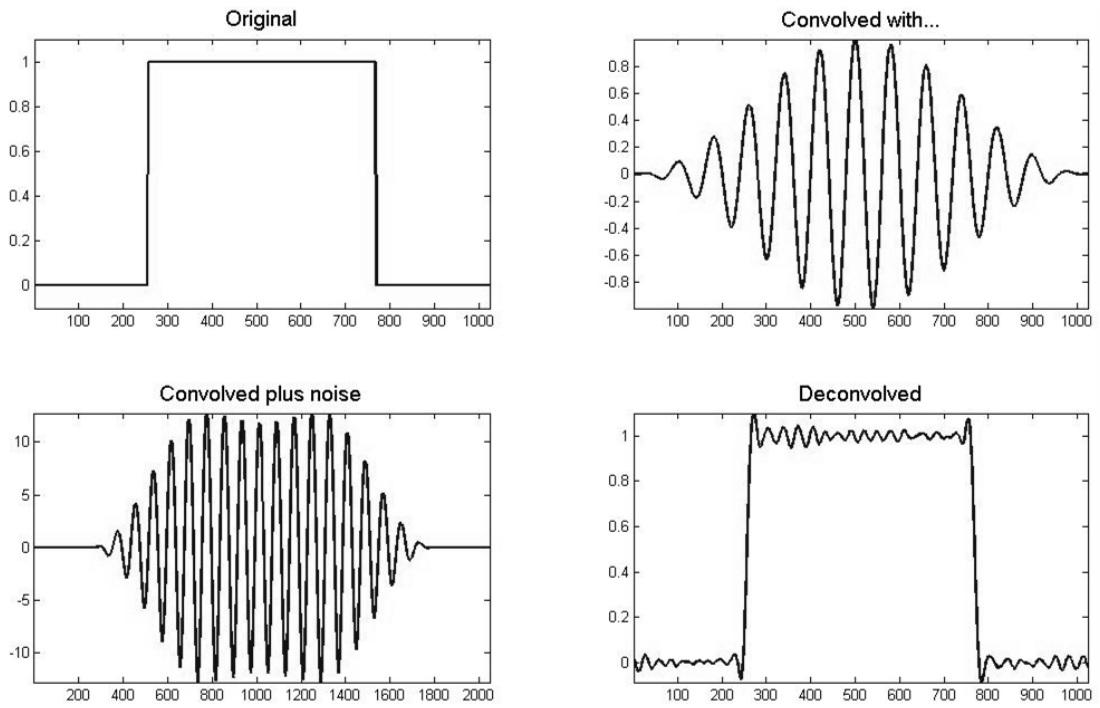

Figure 2.3.8-1: Example of ringing effect in Fourier-domain Wiener deconvolution

2.3.9 Quasi-stationary Approach: Wavelet Shrinkage of the Log-Gabor-Spectrum

Adam and Michailovich mention a quasi-stationary modification to their approach in [1] based on segmentation of the signal, processing each segment under the assumption that it is stationary and then concatenating the results. This quasi-stationary approach can be extended to offer an intermediate solution between the proposed solution and the initial stationary approach described by Adam and Michailovich; Rather than using non-overlapping rectangular-windowed segments, the segments can be windowed and overlapping. Hence, the Gabor transform – the Fourier transform of overlapping Gaussian-windowed segments – and Gabor deconvolution – segment-by-segment Wiener deconvolution and reconstruction – can be used to localize both the pulse estimation and deconvolution with respect to time.

It should be noted that this approach then introduces a trade-off of time-localization – i.e. time-resolution of the quasi-stationary segment spectra – and frequency-resolution in the analysis [8], [23]. Thus, the window length for the Gabor transform is another parameter to select in addition to the wavelet vanishing moments and DWT decomposition level choices present in implementing the stationary method proposed by Adam and Michailovich. Using the quality metrics proposed in Section 4.3 in conjunction with subjective assessment of the image quality, it was found empirically that a window length of 50 samples was suitable for this implementation. Of course, the optimal segment length depends on the sampling frequency, the length of the recorded signals and the non-stationarity of the signals, which is necessarily application dependent.

The quasi-stationary adaptation of Adam and Michailovich's method as implemented in this work follows the steps provided above for the stationary method but replaces the Fourier transform with the Gabor transform. The method can be summarized as follows:

- The log-magnitude-spectrum of each fifty-percent overlapped Gaussian-windowed segment of the signal is calculated;
- The DWT shrinkage and Wiener deconvolution are then applied to each windowed segment spectrum;
- The final result is reconstructed by applying the inverse Fourier transform to each segment, after which the overlapping segments are summed accordingly.

For simplicity, the overlap chosen for the Gabor transform in this method is fifty-percent. As noted in [24], the fifty-percent overlap guarantees near perfect reconstruction when using the Gabor transform.

3. Proposed Log-Scalogram Shrinkage Technique

3.1 Introduction

This work proposes a novel blind deconvolution and denoising method for ultrasound. The proposed method aims to improve on the log-spectrum shrinkage-based method introduced by Adam and Michailovich in [1], which itself was an improvement on the cepstrum-domain approach of Jensen and Leeman in [9]. Using these works as a foundation, the proposed method as covered herein deals with neither the rigorous experimental verification of the pulse spectrum estimation accuracy nor proving its underlying premises such as the minimum-phase assumption. Rather, the proposed method provides an extension of the log-spectrum shrinkage and cepstrum-domain approaches in which the pulse is not assumed to be stationary and some aspects of wavelet denoising are included. Thus, the pulse estimation and deconvolution are localized with respect to time in this method.

Like the pulse estimation methods of [1] and [9], the proposed method of pulse estimation is based on the general premise that the pulse magnitude-spectrum is smooth relative to the jaggedness of the material reflectivity function magnitude-spectrum. Also, like the log-magnitude-spectrum shrinkage-based technique in [1], the proposed method estimates the pulse spectrum by working with the homomorphic signal model in (6) – i.e. the log-magnitude-spectrum of the acquired signal. The difference between the proposed method and the work in [1] is then largely attributed to the representation of the signal spectrum.

3.2 CWT Coefficients as Representation of Spectra

Based on the aforementioned motivation for time-localization, as discussed in Section 2.3.8, the proposed technique employs the CWT across multiple scales to estimate the time-localized spectrum at each discrete-time sample in the acquired signal. As mentioned in Section 2.2.1, an advantage provided by the CWT over the Gabor transform is that there is no trade-off between time-localization and frequency-resolution. The time-localization of the CWT spectra is frequency dependent as the time-domain support of the wavelet varies with the scale [6].

Note that the convolution theorem for the Fourier transform - as used for (5) and (6) from the signal model - does not generally hold for the CWT or even a windowed Short-Time Fourier Transform (STFT) such as the Gabor transform. Therefore, the use of the multi-scale CWT coefficients as a representation of time-localized spectra is more interpretive than mathematically exact. The nature of this generalization is similar to that of the pulse estimation assumptions – that is, a simplified interpretation of complex phenomena rather than rigorous mathematical proof.

3.3 Wavelet Selection

For estimation of the ultrasound pulse the CWT mother wavelet should be selected such that it resembles the pulse in order to provide a sparse representation of the back-scattering information in the acquired data [6]. The Coiflet-2 wavelet was used for the application described in Section 5 and was selected by subjective visual comparison with a pulse in the experiment data. However, while this selection is subjective and is

also dependent on the transducer and imaging system used, it should be noted that the performance of the proposed technique was not sensitive to the wavelet selection – the Coiflet and Symlet wavelets over a range of orders performed similarly with respect to the metrics defined in Section 4.3. As such, the technique should generalize well to other transducer-pulser setups.

The DWT mother wavelet will be selected in agreement with the work in [1]. That is, the Symlet wavelet will be used to decompose the CWT scalogram and separate the smooth pulse spectrum via wavelet shrinkage of the DWT detail coefficients. Likewise, the number of vanishing moments of the mother wavelet and DWT decomposition level will be in agreement with the ranges discussed in [1] and initially will be found empirically.

3.4 Range of Scales for CWT

More importantly however, the CWT scales should match the dominant frequency range of the pulse. The range of CWT scales to be considered can be found by calculating the CWT coefficients in part of the acquired data or by heuristic optimization with respect to some quality metric performed on part of the data set. For example, Fig. 3.4-1 shows the magnitude of the CWT coefficients calculated for scales 1-100, in steps of one, for a single scan-line sampled at 160 MHz containing four reflections. Note that the peak located around discrete-time index 3550 is noise, not a reflection, and its energy spreads over a considerable range of scales. As such, the pulse energy in this case appears to be concentrated around scales 10-30.

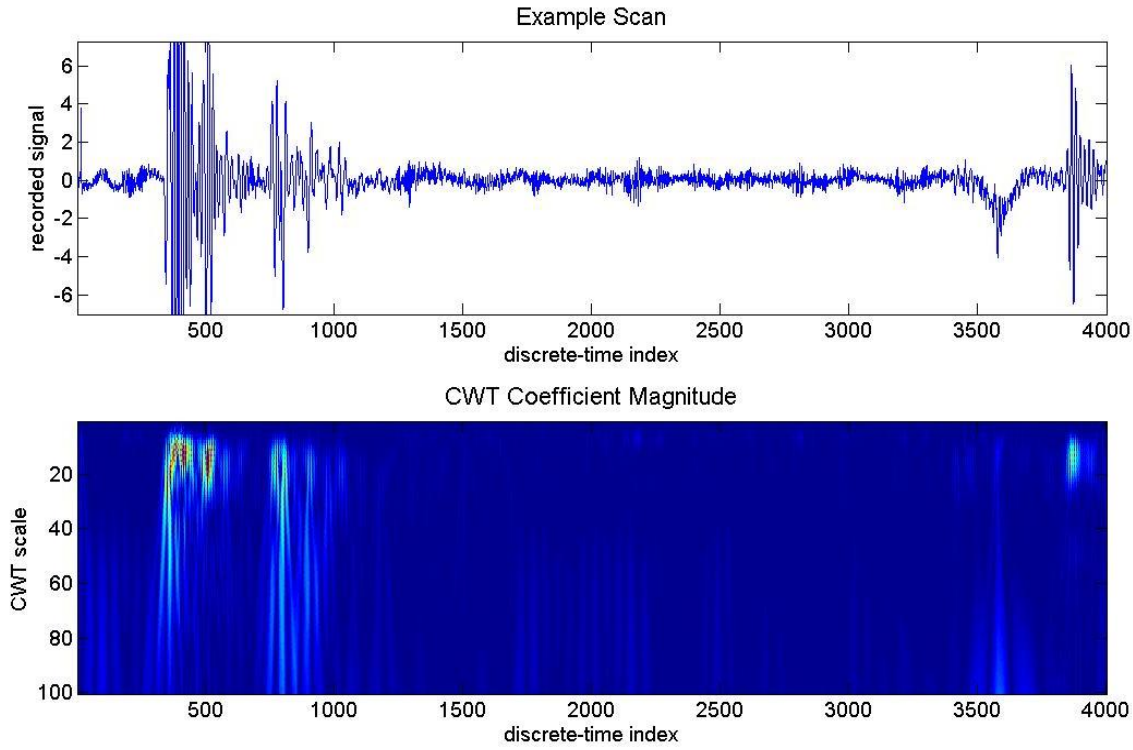

Figure 3.4-1: Example scan (top) and the magnitude of its corresponding CWT-coefficients from scales 1-100 (bottom)

For the purposes of explanation in this section this empirical selection of the CWT scales will suffice. As mentioned above, other parameters such as the DWT wavelet vanishing moments and decomposition level will be in accordance with the ranges suggested in [1] for the Fourier-domain method and found empirically. Automatically selecting the parameters of the proposed technique – CWT scales, Wiener regularization coefficient, DWT wavelet vanishing moments and DWT decomposition level – will be further explored in Section 4 using heuristic optimization with various quality metrics.

3.5 Summary of Method

The proposed log-scalogram shrinkage-based technique for blind deconvolution of ultrasound, as implemented for the application described in Section 5, is summarized as follows:

1. Apply the CWT to the acquired data over the range of scales where pulse information is dominant, in this case ten to thirty in steps of one, using a mother wavelet resembling the pulse such as the Coiflet-2;

   $s(n) \Leftrightarrow S(a,n)$, where a denotes the scale.
2. Calculate the log-magnitude of the CWT coefficients;

   $S(a,n) \Rightarrow \log|S(a,n)|$
3. Apply DWT across the CWT-scales, i.e. in the a-direction, using the Symlet wavelet with six vanishing moments to a decomposition level of three. Note that the number of vanishing moments matches that of the stationary log-spectrum shrinkage method. Similarly, the decomposition level selected is dependent on the range of CWT scales considered.
4. Reconstruct the pulse CWT-coefficients estimate $\log\left|\tilde{G}(a,n)\right|$ from the DWT approximation coefficients and approximate its phase via the Hilbert transform.
5. CWT-domain Wiener deconvolution for each scale:

   $\tilde{H}(a,n) = \frac{S(a,n)\tilde{G}^*(a,n)}{|\tilde{G}(a,n)|^2+\varepsilon}$ where ε is a constant proportional to the noise level.

6. Inverse CWT for each scale, $\widetilde{H}(a,n) \Leftrightarrow \tilde{h}_a(n)$, and arithmetic averaging of the resulting signals, $\tilde{h}(n) = \frac{1}{A}\sum_a \tilde{h}_a(n)$, where A denotes the number of scales considered.

Although the proposed technique can be summarized simply as an extension of the method of Adam and Michailovich to the CWT scalogram rather than a Fourier spectrum, there are interesting consequences to this extension beyond the aforementioned compaction property. The resulting technique, in particular the wavelet-domain Wiener deconvolution filter of the fifth step above, is similar to the WienerChop method of [11] and [12], described in Section 2.2.4. The exception is that the estimate is of the pulse to be deconvolved in the presence of noise rather than the noise-free signal and is found by DWT-shrinkage of the CWT coefficients rather than simple thresholding of the coefficients. The other difference between the proposed technique and the WienerChop method is the use of multiple wavelet bases. However, the proposed technique can be extended to use a second wavelet as in the WienerChop method. The inclusion of a second wavelet for the deconvolution stage is explored in the following subsection.

3.6 WienerChop Modification

The proposed log-scalogram modification to the log-magnitude-spectrum shrinkage-based method of Adam and Michailovich [1] can be further modified to include separate CWT wavelets for the estimation and Wiener deconvolution stages based on the principles of the WienerChop method of [11]. As discussed in Section 2.2.4, the use of a separate wavelet for the deconvolution stage may reduce the effects of

estimation error in the first wavelet domain on the final result. The possible reduction in the effects of estimation error occurs due to spreading of the error over a wider range of wavelet scales in the wavelet deconvolution domain relative to the signal.

This modification to the proposed technique can be implemented by performing steps three and four in the WienerChop summary between steps four and five of the preceding summary of the proposed technique. The estimated pulse CWT coefficients, reconstructed from the DWT approximation coefficients, are converted to time-domain via inverse CWT. The original data and estimated pulse are then transformed to a second CWT domain where the Wiener deconvolution occurs.

For this implementation the second wavelet basis was the Daubechies-2 wavelet, which was selected intuitively to be both sufficiently different than the Coiflet-2 and as a means of enhancing the edges of the final deconvolved image. As mentioned in [12], the influence of the second wavelet is difficult to formulate and as such, the selection was done empirically. To illustrate the effects of including the second wavelet, a comparison will be made in the results in Section 6.3 between the proposed technique with a single CWT basis and that described here incorporating the WienerChop principles.

4. Optimized Parameter Selection

4.1 Introduction

The performance of the proposed log-scalogram shrinkage-based technique in both its one-basis and WienerChop-modified two-basis implementations is obviously dictated by the selection of its parameters. For this work the following parameters will be optimized: DWT wavelet vanishing moments, DWT decomposition level, Wiener regularization coefficient, as well as the CWT minimum and maximum scales. For simplicity the selection of the CWT wavelets will be left unchanged from those noted in Section 3.3. Also, the range of CWT scales will be covered in increments of one limiting the scales to integer values, although the CWT has no restriction on non-integer scales. These exclusions are considered necessary to limit the complexity of the optimization problem since the search space would otherwise grow exponentially. Furthermore, the performance of the method was found to be relatively insensitive to these excluded parameters.

Since the aforementioned parameters essentially control the behaviour of the proposed technique with respect to separation of the pulse and reflectivity function, the reflectivity function would necessarily influence the optimal parameter selection. It will be assumed for simplicity that some overlap of the pulse and reflectivity function is inevitable and thus a compromise is made to either include information regarding the reflectivity function in the pulse estimate or exclude components of the pulse spectrum. Of course, the degree to which this compromise will be made in the parameter

optimization will be assessed by the performance of the proposed technique on a training set with respect to some given cost function.

To facilitate automatic selection of the algorithm parameters, a small number of scans will be used as a training set. In this work only six adjacent scans were used as the training set from the experimental setup described in Section 5. Such a small training set is adequate for this application due to the relative similarity of the scans. If imaging structures with greater scan-to-scan variety of content, a larger training set or content-triggered re-training may be advisable. Only the single CWT wavelet implementation of the proposed technique was used in the parameter selection under the assumption that running the optimization for the WienerChop-modified technique would yield similar parameters.

4.2 Heuristic Optimization

Automated selection of the parameters in the proposed technique may be viewed as an optimization problem given a certain image quality metric and is thus accomplished via heuristic optimization. Such a gradient-free method is required due to the fact that no explicitly defined relation exists to describe the behavior of the proposed technique with respect to each parameter and a given quality metric. Some knowledge of the parameter selection problem does exist to guide the optimization setup, such as a reasonable range of values provided in [1] and the assumption that the performance of the technique is stable with respect to parameter values in that range. As such, it can be assumed that any quality metric will be smooth with respect to each parameter. Given these assumptions, the heuristic optimization was implemented as a five-dimensional

Nelder-Mead simplex direct-search [25]. Boundaries on the simplex search were implemented as penalty factors included in the cost function [25]. Multiple restarts and random seeding points were added to the simplex search for robustness.

4.3 Cost Functions

For a lack of an established quality metric for ultrasound deconvolution and for the sake of comparison, several different cost functions were used to optimize the parameters of the proposed technique: entropy, autocorrelation 6-dB width divided by PSNR and a fractal dimension estimate. Due to the fact that the metrics will only be comparing the same image content processed with different parameters they need not be content independent – i.e. these metrics could not be used to compare the blurriness of several different images with different edges or textures.

Entropy has been commonly used as a quality metric for images and is considered as a measure of the information content [26]. Alternatively, entropy can be viewed as the flatness of a probability distribution. For the purposes of evaluating deblurring and denoising effectiveness, entropy can be calculated directly on the image pixel intensities rather than a histogram – i.e. a sampled probability distribution – as a measure of the edge thickness rather than the probability distribution flatness. Thus, for this application minimum entropy corresponding to sharper edges is desired.

The autocorrelation function of a signal relates how each sample of the signal is correlated to prior and subsequent samples. Specifically, the main lobe of the autocorrelation function, if such a separable lobe exists, corresponds to how small shifts in the signal affect correlation with itself. Thus, if an image is blurred, there will be a

greater correlation along the direction of the blur. The temporal blur is of consideration here and as such, the autocorrelation of the ultrasound scans in the range direction is considered. The degree to which the image is blurred can be described by the width of the main lobe of the autocorrelation function.

Autocorrelation 6-dB width was considered in [27] as a measure of ultrasound image blur. Since the autocorrelation 6-dB width is restricted to an integer value of samples, the cost function is made more sensitive to more subtle improvements by dividing it by its peak signal-to-noise ratio in linear terms. Otherwise it was found that several different parameter settings resulted in the same autocorrelation 6-dB width while the subjective quality of the resulting images varied significantly, particularly with respect to noise levels. Hereafter this cost function, the autocorrelation 6-dB width divided by the PSNR, will be referred to simply as AW&N (autocorrelation width and noise) for brevity.

Fractal dimension used as a measure of image blur is novel to this work. The application of fractal dimension estimates as a measure of blur may not generalize to other types of images due to the fact that in traditional image blurring, such as camera or subject motion in photography, the blurring kernel is smooth and unimodal. In the case of the signal model presented in (4), in which the ultrasound pulse resembles a modulated sinusoid with multiple peaks, the blurring of the reflectivity function introduces repetitions of the image edges as noticeable in the images in Section 6. Note that entropy and autocorrelation main-lobe width only account for the width of the edges, not their repetition as described here. Since fractal dimension estimates are a measure of signal complexity or time-filling property, they can be used in this application to

measure the repetition of image edges [28]. For this work the Katz fractal dimension estimate is used. While many means of estimating the fractal dimension of a signal exist, the Katz estimate is less sensitive to noise than the Higuchi estimate, for instance. Also, the Katz fractal dimension estimate can be calculated directly on the waveform without the requirement of preprocessing [29].

The fractal dimension of a signal can be defined as:

$$D = \frac{\log_{10}(L)}{\log_{10}(d)} \tag{30}$$

"*where L is the total length of the curve or sum of distances between successive points, and d is the diameter estimated as the distance between the first point of the sequence and the point of the sequence that provides the farthest distance*" [29]. Of course, the distances here are dependent on the units of measurement – i.e. the amplitude and time scales. The Katz fractal dimension corrects for this dependency by normalizing both L and d with respect to the average distance between successive samples, denoted here as a. The Katz fractal dimension is then given as:

$$D = \frac{\log_{10}(L/a)}{\log_{10}(d/a)} \tag{31}$$

Then considering the total number of samples in the signal, n, for which $n = L/a$, (31) can be expressed equivalently as:

$$D = \frac{\log_{10}(n)}{\log_{10}(d/L)+\log_{10}(n)} \tag{32}$$

The parameter selections resulting from the use of the aforementioned cost functions are listed in Table 4.3-1. Note that some parameters are less influential on the

behavior of the proposed technique than others – i.e. different CWT scale range selections produced visually noticeable differences in the final image while in comparison the DWT decomposition level produced little change. Thus, the parameter selections alone are not necessarily indicative of the influence of the various cost functions. Further discussion follows in Section 6.

Table 4.3-1: Parameters Selected with Various Cost Functions

	Empirical	Entropy	AW&N	Fractal Dimension
Vanishing moments	6	9	2	9
Decomposition level	3	9	7	8
Regularization coefficient	2000	2037	3482	1510
Minimum CWT scale	10	8	15	15
Maximum CWT scale	30	18	31	40

5. Experiment

A section of an underground power cable, similar to that shown in Fig. 5-1, was immersed in a water tank and imaged in two-dimensions by scanning around its circumference with the transducer approximately radially aligned with the cable – i.e. the line of sight of the transducer was roughly perpendicular to the cable surface both circumferentially and along its length.

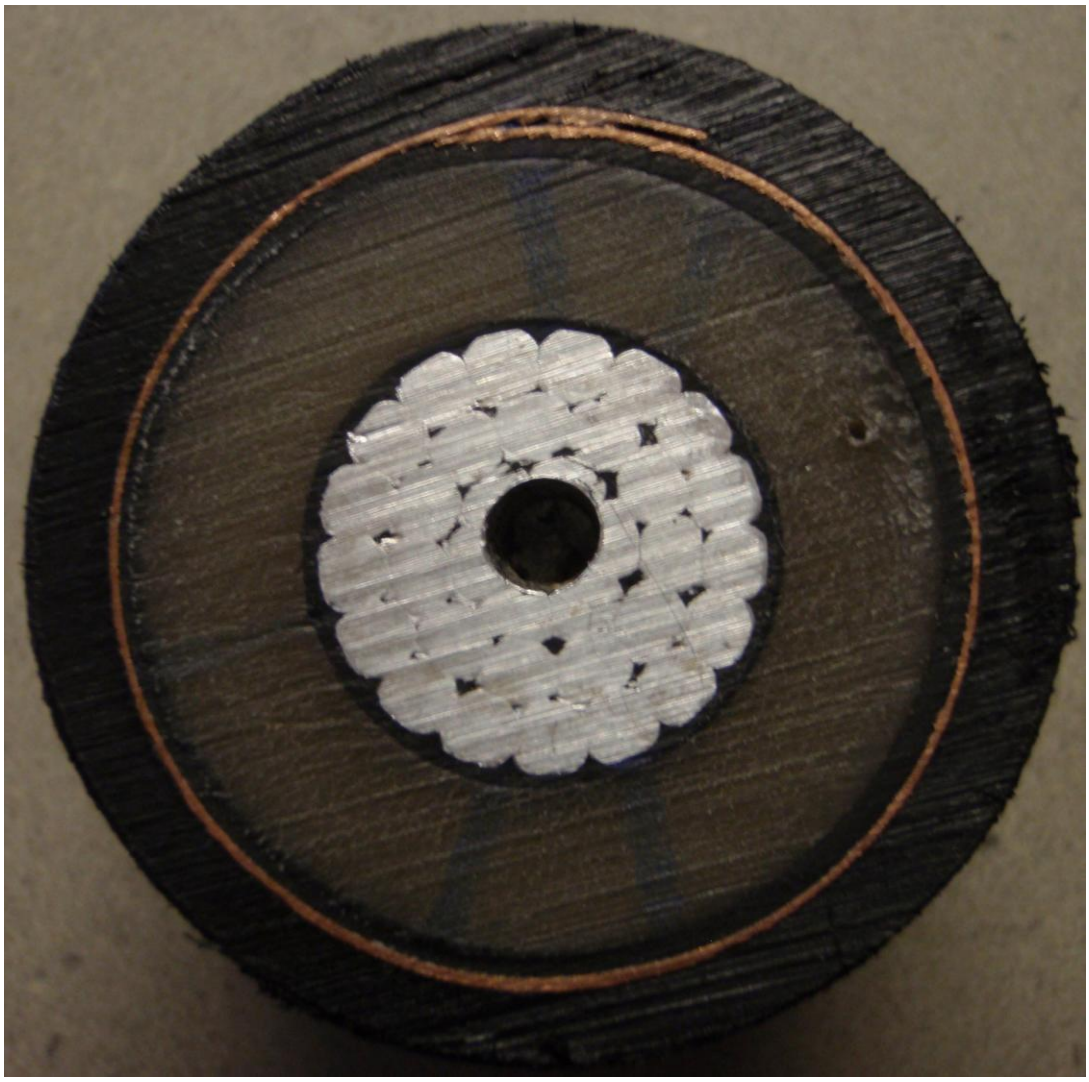

Figure 5-1: Cross-sectional photo of power cable (enlarged)

Alignment of the cable and transducer was performed manually via visual inspection. To correct for this as well as any surface imperfections or non-circularity of the cable the scans were aligned prior to forming the circular images shown in the next section. Due to the “blurriness” and noise in the raw scan data, alignment had to first be performed on the scans processed by the proposed technique. Temporal alignment of the scans was performed by cross-correlating each scan with the first scan and subsequently

shifting by the location of the cross-correlation maxima from center. These same shifts were then applied to all the images.

The transducer used was a General Electric 15 MHz non-focused immersion transducer, model number 113-127-300 (as documented in Appendix A). A Lecoeur Electronique US-Key pulser (Appendix B) was used to drive the transducer and interface with a computer, from which the data acquisition and analysis were performed with MathWorks MATLAB software. The sampling frequency used was 160 MHz.

In order to highlight the effectiveness of the noise removal properties in the proposed method and compare with that of the other methods, no averaging was done between multiple scans at the same position. That is, only one scan was recorded per angular position around the cable. While AWGN could otherwise be reduced by averaging multiple scans per position, this at least demonstrates the stability or insensitivity of the method in low SNR applications.

All of the imaging in this work took place in the near-field of the aforementioned transducer. Near-field imaging was necessary due mostly to the size of the transducer, which was selected due to the acoustic power required to propagate through the multiple layers of the cable. Furthermore, the future development of a field-ready test setup for industrial application limits the distance that the transducer can be placed away from the cable. That is, far-field imaging would theoretically be possible by moving the transducer further away, as given by equation (2), however, practically the test setup should be more compact to allow mobility of the transducer down the length of the cable being tested.

6. Results and Discussion

The results will be organized in three subsections. The first will compare the initial implementation of the proposed technique with manually selected parameters to its preceding methods: the stationary log-magnitude-spectrum shrinkage technique proposed by Adam and Michailovich, and the intermediate solution, its modification using the Gabor transform. Second, the effects of parameter optimization will be examined with respect to the various cost functions presented in Section 4.3. Last, the use of a second CWT basis similar to the WienerChop method will be explored. Additional discussion follows.

For visual clarity in the results all images are truncated in time-duration of the scans and some details of the inner cable, namely the XLPE layer, are omitted. This is due to the fact that the XLPE layer features very little detail in contrast to the first few layers of the cable, which better exhibit the effectiveness of the technique. Furthermore, since the presence of water-trees in the tested sample is unknown, the experiment as documented here is more aimed at a general pre-processing of ultrasound rather than the specific application of water-tree imaging.

Images are shown approximately aligned in rotation with the cable photo in Fig. 5-1, as seen by noting the position of the overlap in the copper layer at the top of the image. However, due to the propagation velocity differences in each material the layer-to-layer edges are not aligned with Fig. 5-1. The unprocessed ultrasound B-scan image is shown in Fig. 6-1.

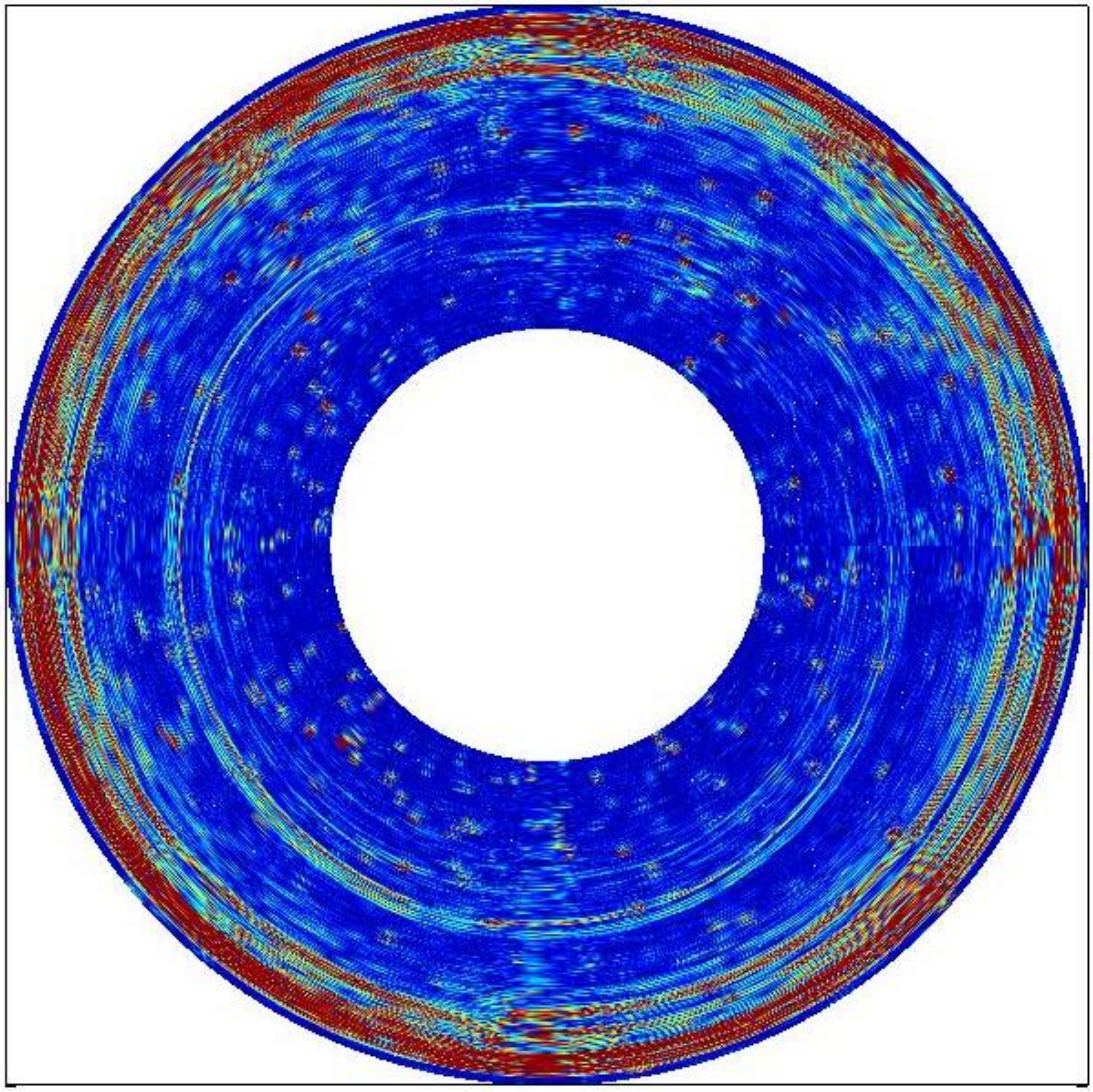

Figure 6-1: Unprocessed B-scan image

6.1 Proposed Technique vs. Log-Spectrum Shrinkage Method

Fig. 6.1-1 - 6.1-3 show the results of deconvolution using the stationary log-spectrum shrinkage, quasi-stationary log-spectrum shrinkage, and the proposed technique with empirically selected parameters and a single CWT basis, respectively.

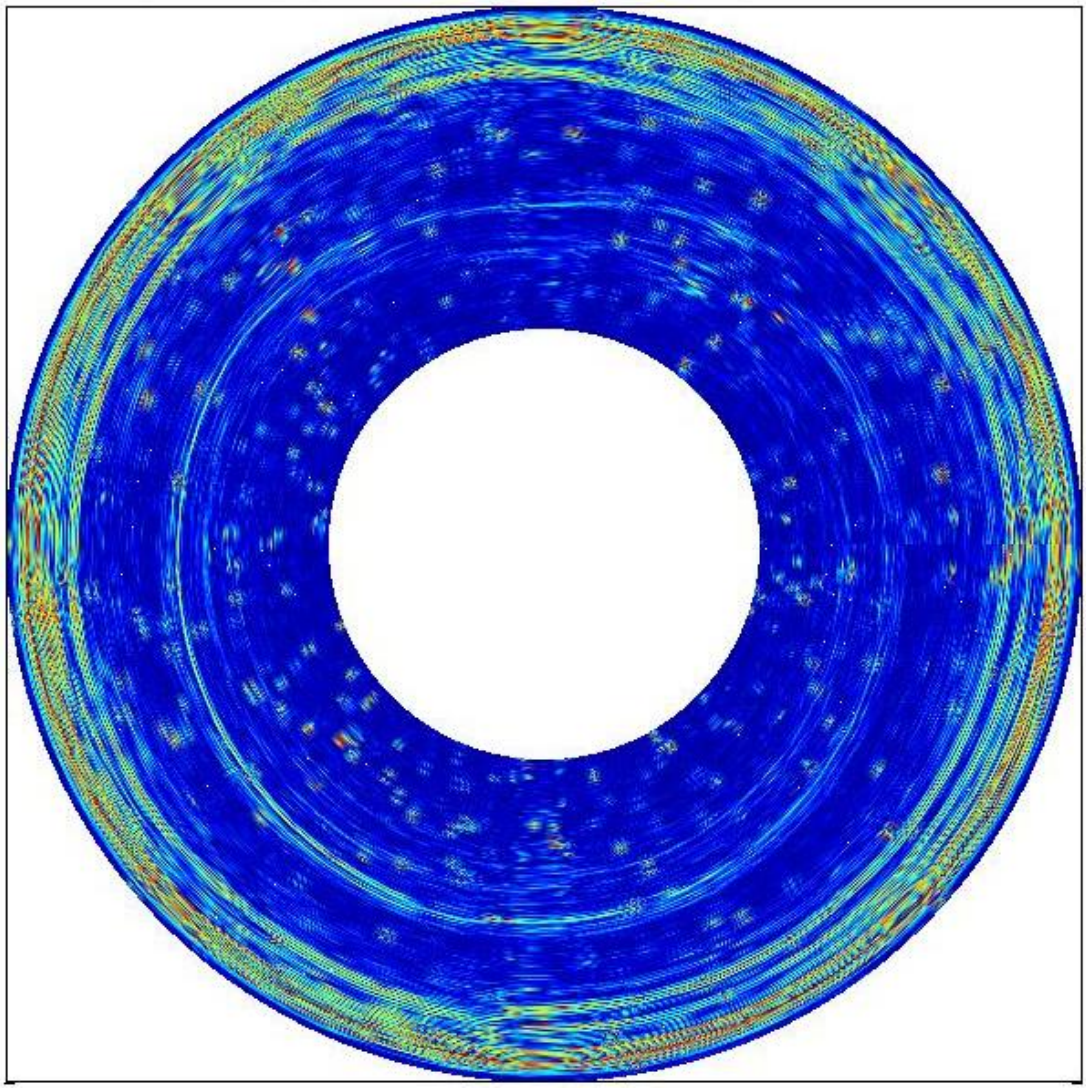

Figure 6.1-1: Results of stationary log-spectrum shrinkage-based deconvolution

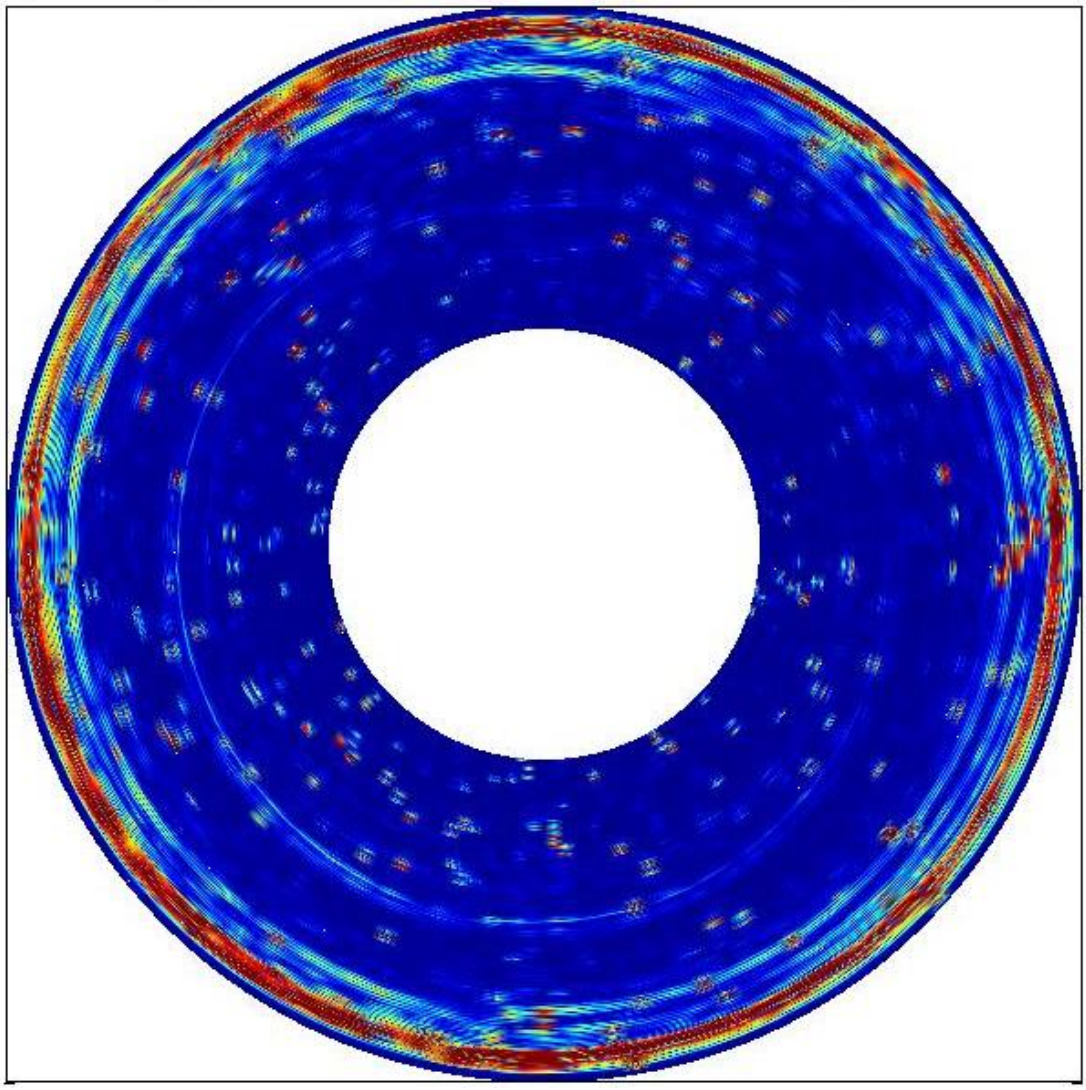

Figure 6.1-2: Results of quasi-stationary log-spectrum shrinkage-based deconvolution

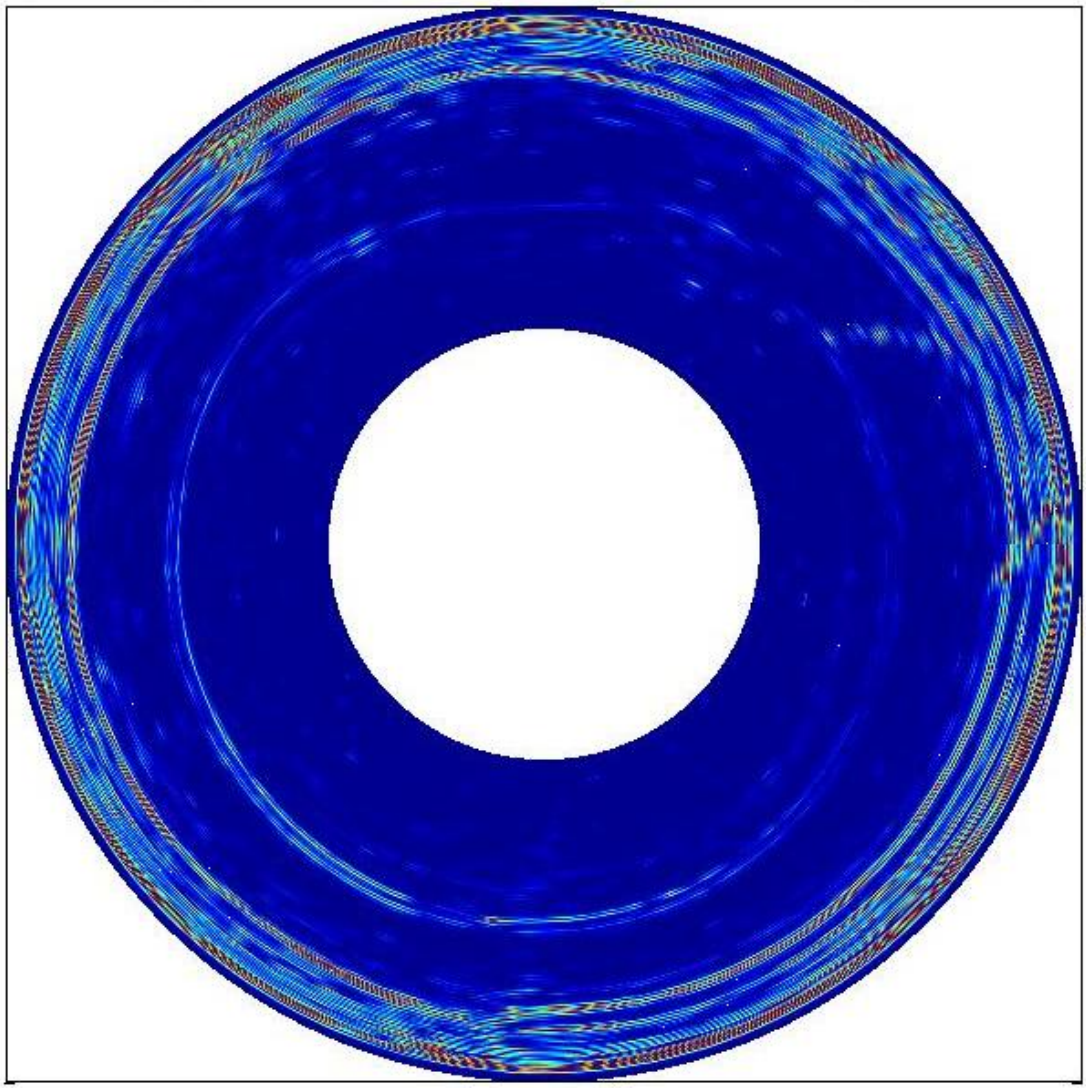

Figure 6.1-3: Results of proposed log-scalogram shrinkage-based deconvolution with empirically selected parameters and a single CWT basis

Visually assessing the results, the stationary log-spectrum shrinkage offers only a slight improvement on the unprocessed image. The quasi-stationary log-spectrum shrinkage processed image, while noticeably different than the unprocessed image, is not necessarily improved since the larger peaks of noise are still prominent and the edges of the image appear even blurrier. The proposed technique visually reduced noise and

sharpened the edges, which is particularly notable in the separation between the two outermost edges of the image. The quality metrics for the three deconvolution techniques considered, as applied to the above images, are summarized in Table 6.1-1.

Table 6.1-1: Quality Metric Comparison of Methods

	Entropy	AW&N	Fractal Dimension
Unprocessed image	10.98	28.03	1.0317
Stationary log-spectrum shrinkage	11.02	13.53	1.0330
Quasi-stationary log-spectrum shrinkage	9.79	6.59	1.0000
Proposed technique - empirically selected parameters - single CWT basis	8.54	0.48	1.0047

6.2 Parameter Optimization

Fig. 6.2-1 - 6.2-3 show the results of parameter optimization on the proposed technique with a single CWT basis using the cost functions: entropy, AW&N and fractal dimension, respectively.

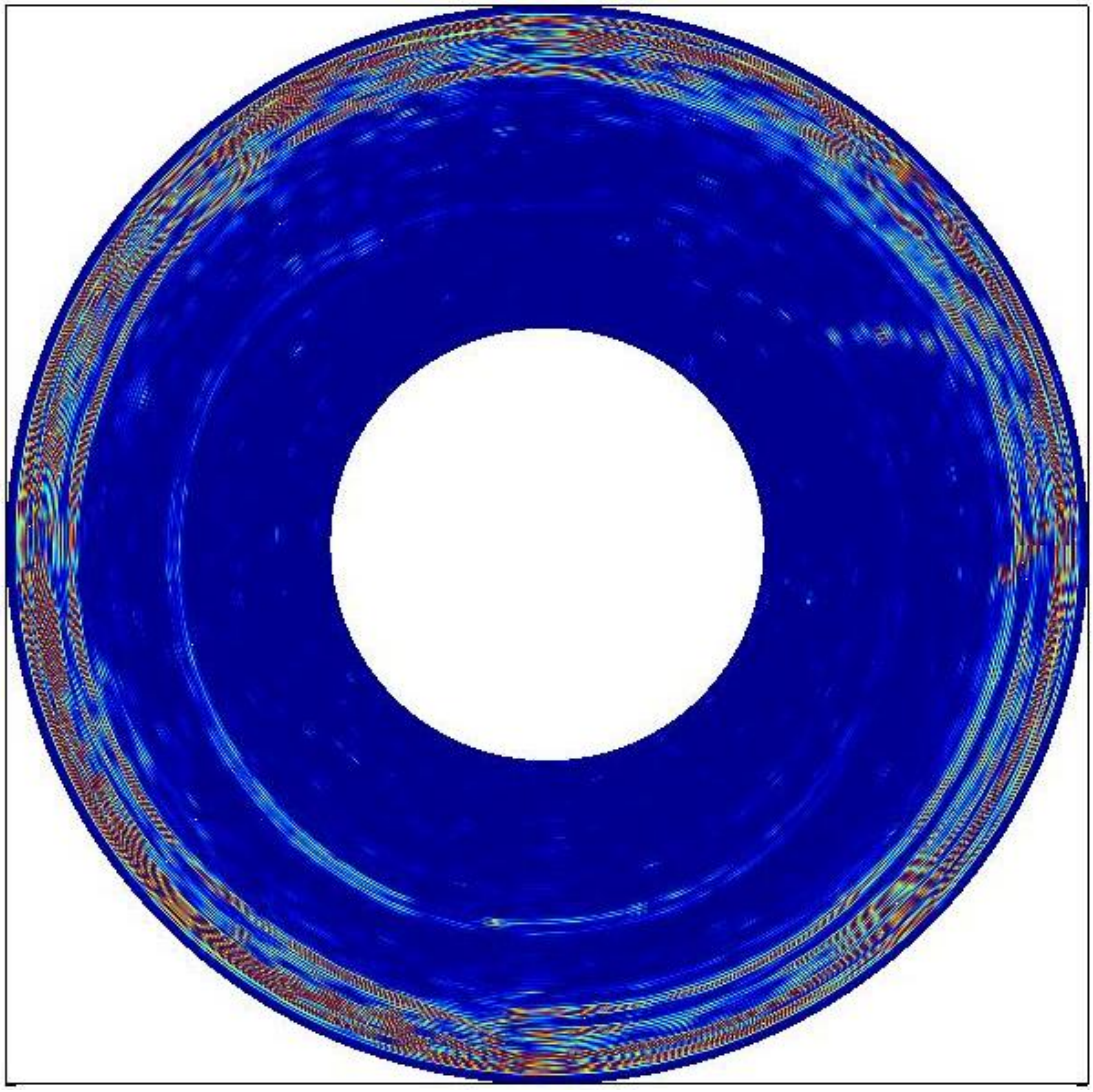

Figure 6.2-1: Results of proposed log-scalogram shrinkage-based deconvolution with entropy-optimized parameters and a single CWT basis

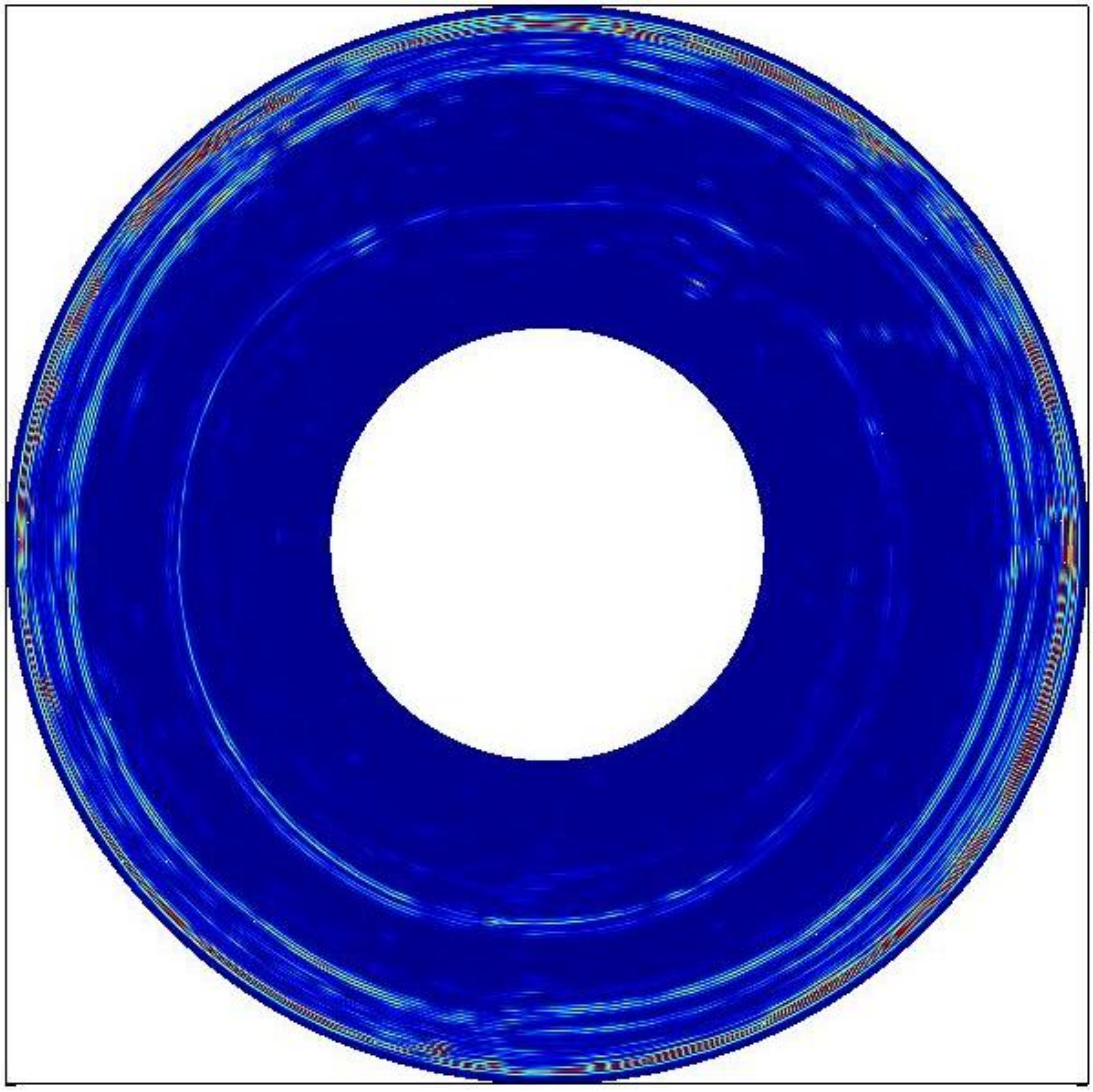

Figure 6.2-2: Results of proposed log-scalogram shrinkage-based deconvolution with AW&N-optimized parameters and a single CWT basis

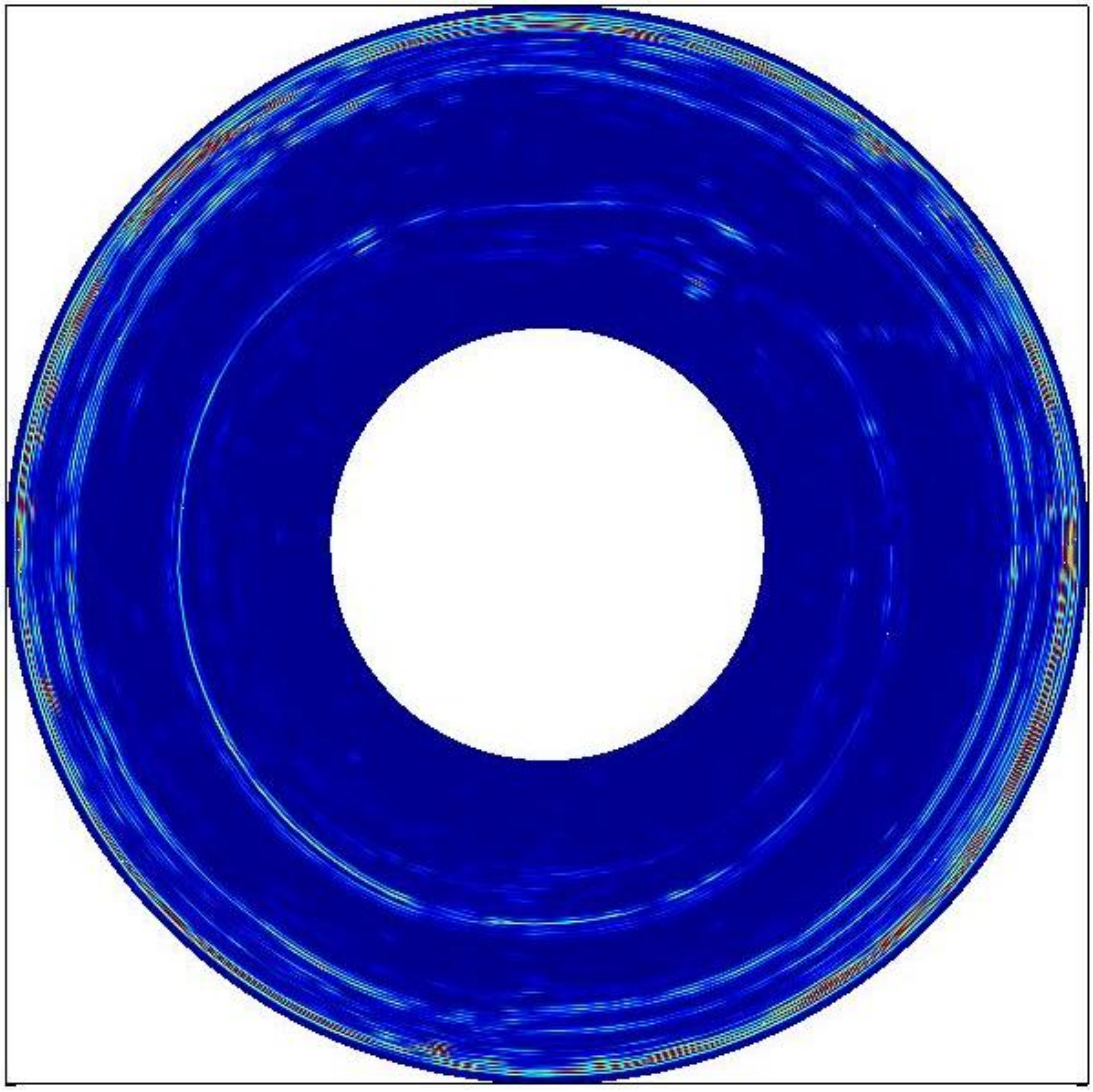

Figure 6.2-3: Results of proposed log-scalogram shrinkage-based deconvolution with fractal dimension-optimized parameters and a single CWT basis

The quality metrics for the single CWT basis cost-optimized processed images are summarized in Table 6.2-1. Visually assessing the results, the fractal dimension and AW&N-optimized parameters produced the clearest images – the two outermost edges are sharper and there is less noise than in the entropy-optimized image – and both represent a noticeable improvement from the manually selected parameters. The entropy-

optimized image is also noticeably noisier and blurrier than that produced by the manually selected parameters, which is in agreement with its higher AW&N and fractal dimension. This indicates the entropy cost function is poorly suited for this application.

Table 6.2-1: Quality Metrics for Cost-Optimized Single CWT-Basis Images

	Entropy	AW&N	Fractal Dimension
Entropy-optimized	8.39	0.61	1.0050
AW&N-optimized	8.40	0.34	1.0040
Fractal dimension-optimized	8.61	0.41	1.0037

6.3 WienerChop Modification

The proposed technique was also implemented using two CWT wavelets, as specified in Section 3.6. Fig. 6.3-1 - 6.3-3 display the resulting images of the WienerChop modified proposed technique using the parameters optimized with respect to entropy, AW&N and fractal dimension, respectively.

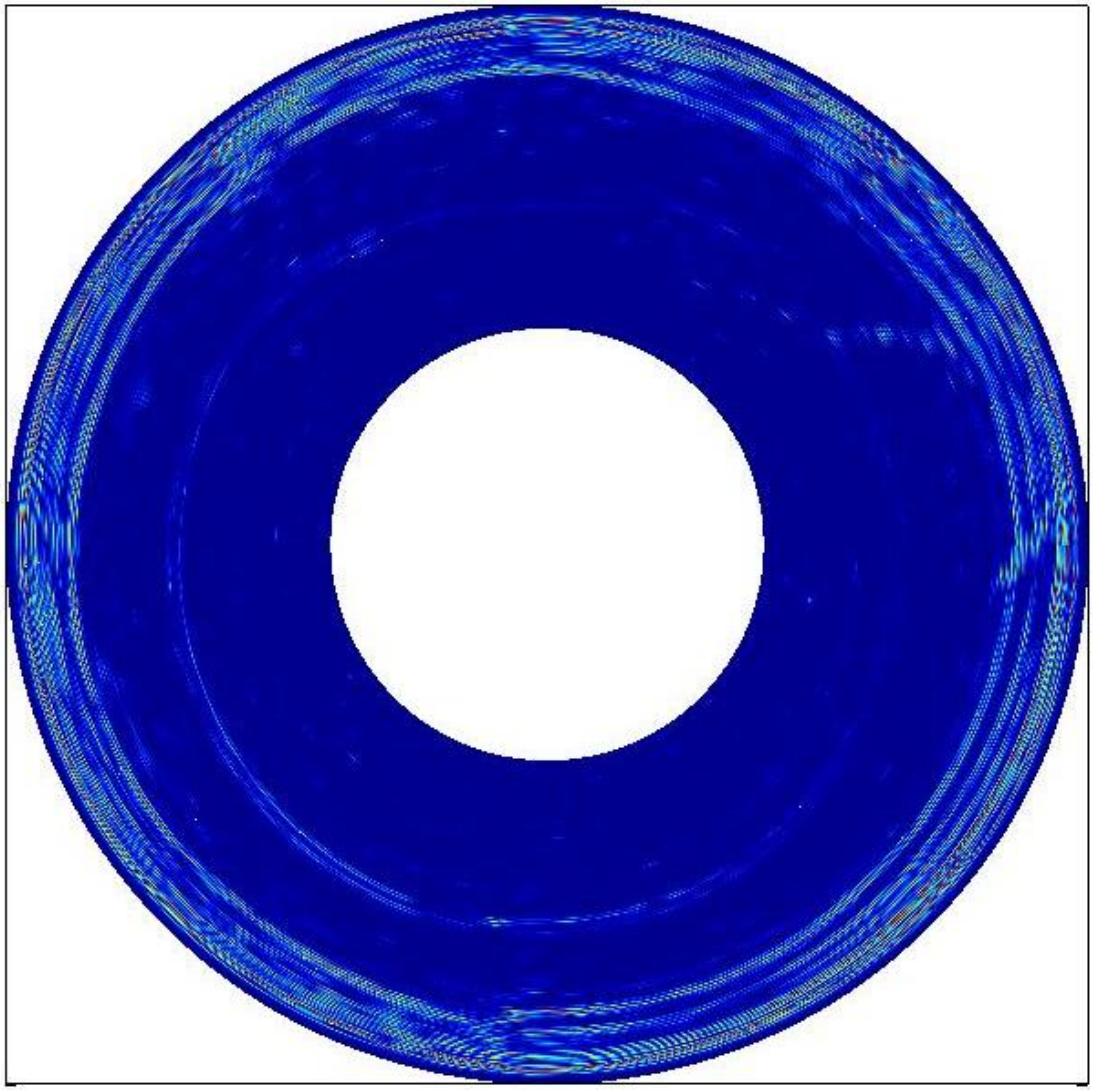

Figure 6.3-1: Results of proposed log-scalogram shrinkage-based deconvolution with entropy-optimized parameters and dual CWT basis

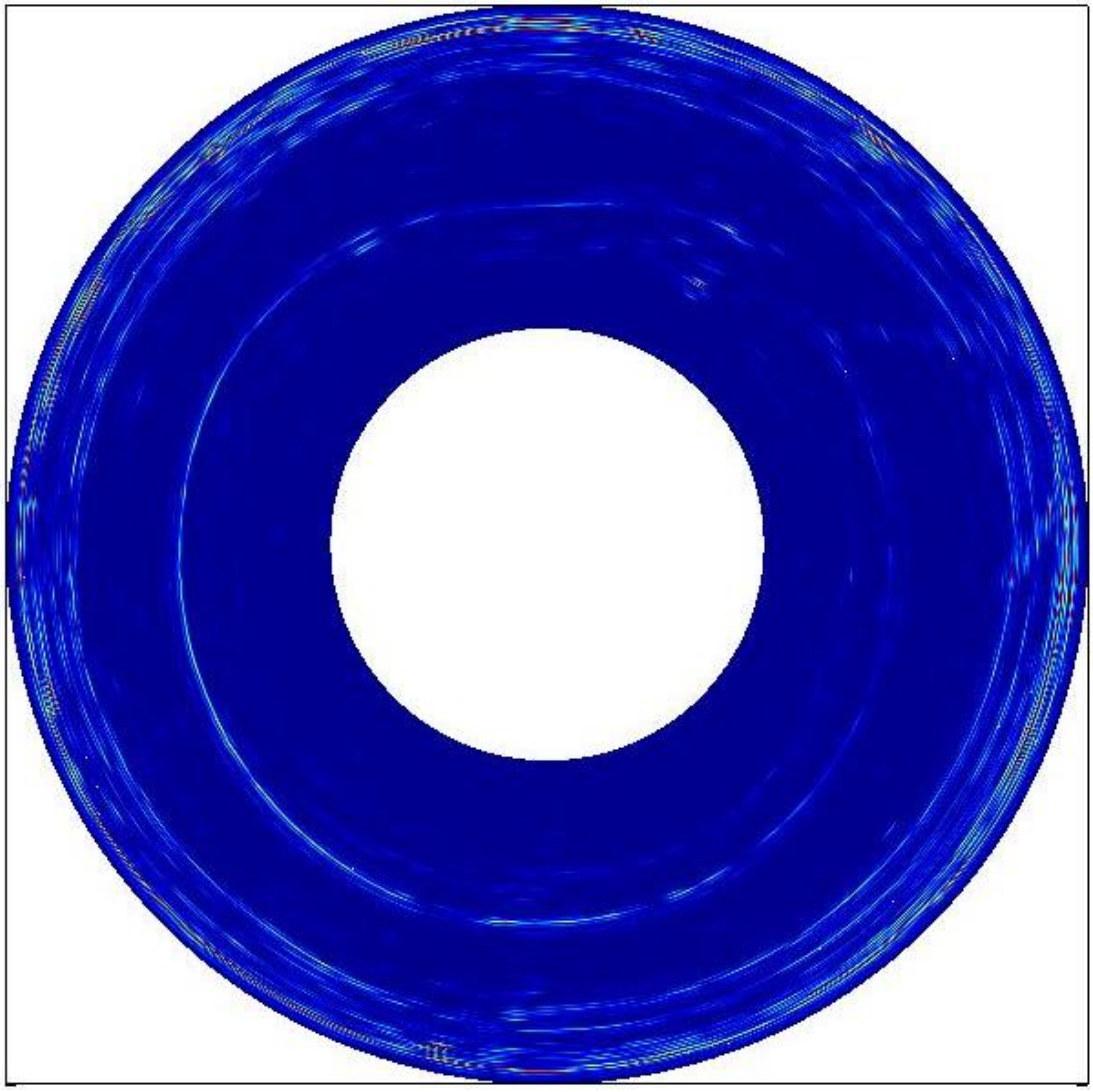

Figure 6.3-2: Results of proposed log-scalogram shrinkage-based deconvolution with AW&N-optimized parameters and dual CWT basis

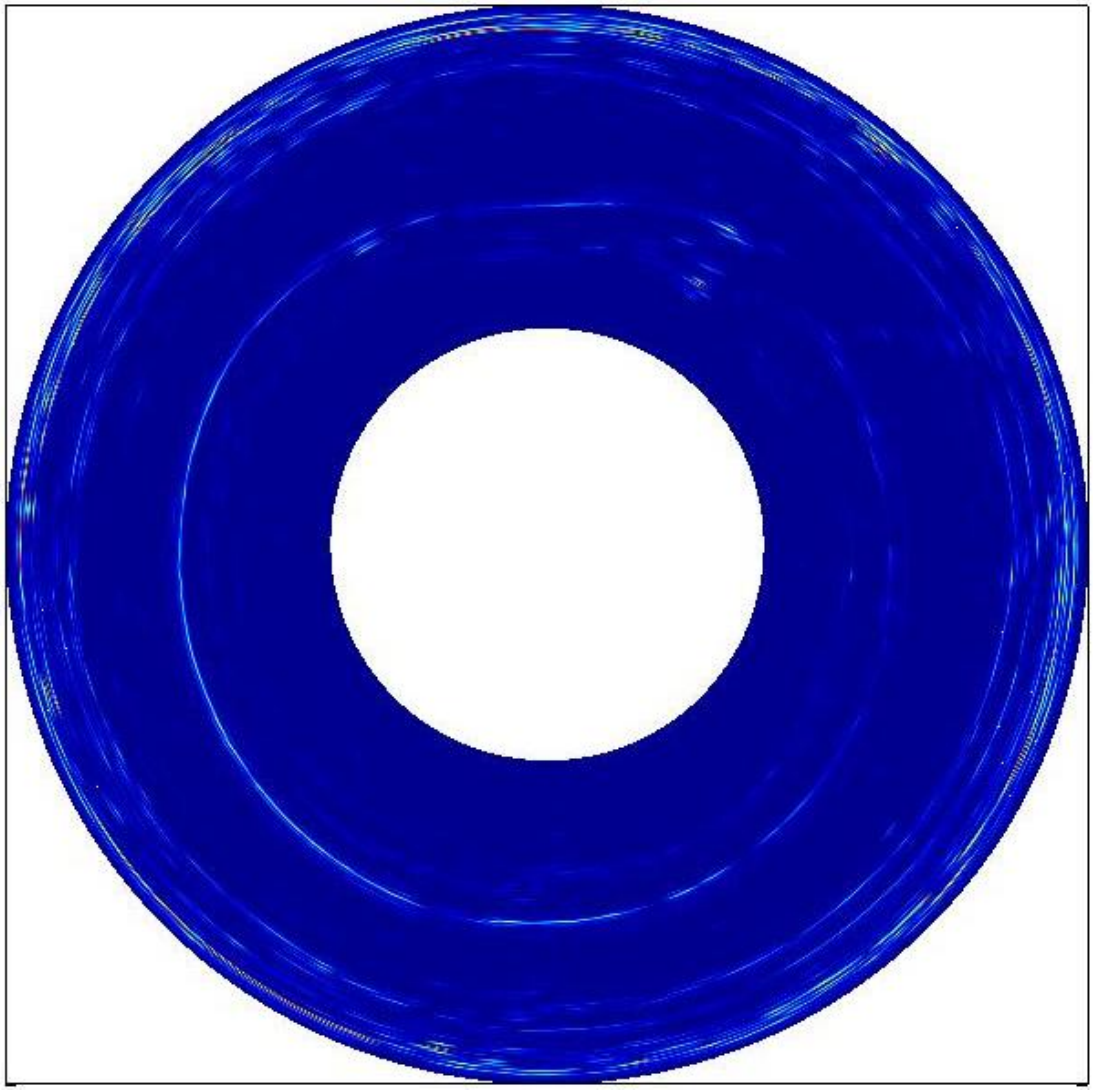

Figure 6.3-3: Results of proposed log-scalogram shrinkage-based deconvolution with fractal dimension-optimized parameters and dual CWT basis

The quality metrics for the dual CWT basis images in Fig. 6.3-1 - 6.3-3 are shown in Table 6.3-1. Assessing the images visually, the fractal dimension-optimized parameters yielded the clearest image with the AW&N-optimized parameters producing similar results. Once again, the entropy-optimized parameters produced a noisier and blurrier image than the other two cost functions. All three images are improved over

their single CWT basis counterparts, illustrating the effectiveness of incorporating the WienerChop principles. Also noteworthy is that the fractal dimension-optimized parameters outperformed the AW&N-optimized parameters with respect to AW&N. This is due to the fact that the parameter optimizations occurred on the single CWT basis implementation and were not repeated for this implementation for which the optimal parameters may differ. An equally likely scenario is that the simplex search returns sub-optimal parameters or that the optimal parameters on the training set are not perfectly matched to the entire image. In either case, the results of the optimization offer adequate enough results to illustrate the effectiveness of the technique.

Table 6.3-1: Quality Metrics for Cost-Optimized Dual CWT-Basis Images

	Entropy	AW&N	Fractal Dimension
Entropy-optimized	8.37	0.23	1.0082
AW&N-optimized	8.56	0.24	1.0036
Fractal dimension-optimized	8.64	0.23	1.0029

6.4 Additional Discussion

Referring back to the parameters in Table 4.3-1 and their resulting images from single and dual CWT basis implementations in Fig. 6.2-1 - 6.2-3 and Fig. 6.3-1 - 6.3-3 respectively, the effects of each parameter or the sensitivity of its setting on the performance of the technique can be seen. For instance, the AW&N and fractal dimension cost functions yielded different DWT wavelet vanishing moments and Wiener regularization coefficients yet produced results of similar quality and characteristics throughout. Moreover, the entropy and fractal dimension-optimized parameters were

similar in their DWT vanishing moments, DWT decomposition level and Wiener regularization coefficient, yet the entropy-optimized parameters consistently produced notably worse results. Thus, as hypothesized in Section 3.4, the range of CWT scales is the most sensitive parameter to select. Recalling that CWT scale is inversely proportional to wavelet pseudo-frequency, the minimum scale can be considered the high-frequency cut-off in the pulse estimation, above which additive noise is more prominent than pulse components. This may explain why the minimum CWT scale in each parameter set was consistently related to the subjective image quality. The fact that the maximum CWT scale could differ so greatly between the AW&N and fractal dimension-optimized values while producing similar results is due to two reasons: that the CWT scale to pseudo-frequency relation is non-linear, resulting in a smaller difference in the actual low-frequency cut-off considered; and that the entire frequency range in which the pulse components were dominant need not be captured due to the over-complete description provided by the CWT scalogram.

7. Conclusion

This thesis presented a novel technique for blind deconvolution and denoising of ultrasound for NDT purposes. Improvements offered by the proposed technique over existing blind deconvolution techniques for ultrasound are primarily based on dealing with non-stationarity of the ultrasound signal, in particular the point-spread function in near-field imaging.

Jensen and Leeman proposed estimating the pulse from the received ultrasound data based on the premise that the pulse magnitude-spectrum was smooth relative to the material reflectivity function magnitude-spectrum. This same premise was used again by Adam and Michailovich, who improved the pulse spectrum estimation via DWT shrinkage of the log-magnitude-transformed Fourier-spectrum of the received ultrasound signal.

Taking the method of Adam and Michailovich as its foundation, the proposed method in this work localized the spectra with respect to time such as to better deal with non-stationarity of the signals. The time-localized spectrum was represented as the multiscale CWT coefficients.

The CWT coefficient magnitudes of the pulse were estimated by DWT shrinkage of the ultrasound signals log-magnitude-transformed CWT coefficients. The phase of the CWT coefficients was recovered via the Hilbert transform, utilizing the minimum-phase assumption that Jensen and Leeman found to be true for most piezoelectric transducers.

The estimated pulse was then deconvolved via Weiner filter in the CWT-domain and the inverse CWT was employed to recover the approximate reflectivity function.

Further improvements were provided by the proposed technique via parameter optimization with respect to the presented cost functions – entropy, autocorrelation width divided by PSNR, and fractal dimension – as well as by utilizing different CWT wavelets for the tasks of estimation and deconvolution, as proposed in the WienerChop algorithm. For the application of power cable imaging, all implementations of the proposed technique offered noticeable improvements over its predecessors with respect to both edge sharpness and noise levels.

References

[1] D. Adam, and O. Michailovich, "Blind deconvolution of ultrasound sequences using nonparametric local polynomial estimates of the pulse," Biomedical Engineering, IEEE Transactions on, vol. 49, no. 2, pp. 118-131, Feb. 2002

[2] Fernandez-Caballero, and J. L. Mateo, "Methodological approach to reducing speckle noise in ultrasound images," Biomedical Engineering and Informatics, International Conference on, vol. 2, pp. 147-154, 27-30 May 2008

[3] D. L. Donoho, and I. M. Johnstone, "Threshold selection for wavelet shrinkage of noisy data," Engineering in Medicine and Biology Society, 1994. Engineering Advances: New Opportunities for Biomedical Engineers. Proceedings of the 16th Annual International Conference of the IEEE, vol. 1, pp. A24-A25, 3-6 Nov 1994

[4] R.K. Mukkavilli, J.S. Sahambi, and P.K. Bora, "Modified homomorphic wavelet based despeckling of medical ultrasound images," Electrical and Computer Engineering, 2008. CCECE 2008. Canadian Conference on, pp. 887-890, 4-7 May 2008

[5] J. L. San Emeterio, and M. A. Rodriguez-Hernandez, "Wavelet denoising of ultrasonic A-scans for detection of weak signals," Systems, Signals and Image Processing (IWSSIP), 2012 19th International Conference on, pp. 48-51, 11-13 April 2012

[6] M. Unser, "Wavelets, statistics, and biomedical applications," Statistical Signal and Array Processing, Proceedings, 8th IEEE Signal Processing Workshop on, pp. 244-249, 24-26 Jun 1996

[7] Q. Xu, S. Wan, W. Pei, and L. Yang, "Ultrasonic image processing using wavelet based deconvolution," Neural Networks and Signal Processing, Proceedings of the 2003 International Conference on, vol. 2, pp. 1013- 1016, 14-17 Dec. 2003

[8] J.-D. Aussel, and J.-P. Monchalin, "Structure noise reduction and deconvolution of ultrasonic data using wavelet decomposition (ultrasonic flaw detection)," Ultrasonics Symposium, Proceedings, IEEE 1989, vol. 2, pp. 1139-1144, 3-6 Oct 1989

[9] J. A. Jensen, and S. Leeman, "Nonparametric estimation of ultrasound pulses," Biomedical Engineering, IEEE Transactions on, vol. 41, no. 10, pp. 929-936, Oct. 1994

[10] J. Biemond, R. L. Lagendijk, and R. M. Mersereau, "Iterative methods for image deblurring," Proceedings of the IEEE, vol. 78, no. 5, pp. 856-883, May 1990

[11] S. P. Ghael, A. M. Sayeed, and R. Baraniuk, “Improved Wavelet Denoising via Empirical Wiener Filtering,” Proceedings of SPIE, vol. 3169, pp. 389-399, San Diego, July 1997

[12] C. Hyeokho, and R. Baraniuk, "Analysis of wavelet-domain Wiener filters," Time-Frequency and Time-Scale Analysis, 1998. Proceedings of the IEEE-SP International Symposium on, pp. 613-616, 6-9 Oct 1998

[13] G. Thomas, D. Flores-Tapia, S. Pistorius, and N. Fernando, "Synthetic aperture ultrasound imaging of XLPE insulation of underground power cables," Electrical Insulation Magazine, IEEE, vol. 26, no. 3, pp. 24-34, May-June 2010

[14] G. Thomas, D. Flores-Tapia, and S. Pistorius, "Frequency compounding of synthetic aperture ultrasound imagery using multiscale products," Instrumentation and Measurement Technology Conference, 2010 IEEE, pp. 702-705, 3-6 May 2010

[15] J. A. Jensen, "Simulation of advanced ultrasound systems using Field II," Biomedical Imaging: Nano to Macro, 2004 IEEE International Symposium on, vol. 1, pp. 636- 639, 15-18 April 2004

[16] J. A. Jensen, and N. B. Svendsen, "Calculation of pressure fields from arbitrarily shaped, apodized, and excited ultrasound transducers," Ultrasonics, Ferroelectrics and Frequency Control, IEEE Transactions on, vol. 39, pp. 262-267, 1992

[17] A. Graps, "An introduction to wavelets," Computational Science & Engineering, IEEE, vol. 2, no. 2, pp. 50-61, Summer 1995

[18] X. Wang, Y. Shen, Z. Liu, Q. Wang, "Noise reduction for Doppler ultrasound signal based on cycle-spinning and thresholding methods," Instrumentation and Measurement Technology Conference, Proceedings of the 21st IEEE, vol. 3, pp. 1922- 1925, 18-20 May 2004

[19] M. Unser, "Vanishing moments and the approximation power of wavelet expansions," Image Processing, Proceedings, International Conference on, vol. 1, pp. 629-632, 16-19 Sep 1996

[20] J. G. Proakis and D. Manolakis, “Inverse Systems and Deconvolution” in Digital Signal Processing: Principles, Algorithms and Applications, 3rd ed. New Jersey, Prentice Hall, 1995, ch. 4, sec. 6, pp. 356-361

[21] A. Lopez Sanchez, and L. W. Schmerr, “Characterization of an Ultrasonic Nondestructive Measurement System”, 27 Oct 2006

[22] C. N. Liu, M. Fatemi, and R. C. Waag, "Digital Processing for Improvement of Ultrasonic Abdominal Images," Medical Imaging, IEEE Transactions on, vol. 2, no. 2, pp. 66-75, June 1983

[23] E. Oruklu, S. Aslan, and J. Saniie, "Applications of time-frequency distributions for ultrasonic flaw detection," Ultrasonics Symposium (IUS), 2009 IEEE International, pp. 2000-2003, 20-23 Sept. 2009

[24] G. Thomas, and A. E. Brito, "Noise suppression and component extraction of underwater acoustic signals," OCEANS '97. MTS/IEEE Conference Proceedings, vol. 2, pp. 1353-1358, 6-9 Oct 1997

[25] J. W. Bandler, "Optimization Methods for Computer-Aided Design," Microwave Theory and Techniques, IEEE Transactions on, vol. 17, no. 8, pp. 533- 552, Aug 1969

[26] G. Thomas, B. C. Flores, and D. Flores-Tapia, "ISAR motion compensation using entropy metrics," Radar Systems, 2007 IET International Conference on, pp. 1-4, 15-18 Oct. 2007

[27] J. R. B. Taylor, J. J. M. Chan, and G. Thomas, "Frequency selection for compounding synthetic aperture ultrasound images," Imaging Systems and Techniques, 2012 IEEE International Conference on, pp. 74-77, 16-17 July 2012

[28] S. P. Arjunan, and D. K. Kumar, "Fractal Based Modelling and Analysis of Electromyography (EMG) To Identify Subtle Actions," Engineering in Medicine and Biology Society, 2007, 29th Annual International Conference of the IEEE, pp. 1961-1964, 22-26 Aug. 2007

[29] R. Esteller, G. Vachtsevanos, J. Echauz, and B. Litt, "A comparison of waveform fractal dimension algorithms," Circuits and Systems I: Fundamental Theory and Applications, IEEE Transactions on, vol. 48, no. 2, pp. 177-183, Feb 2001

Appendix A: Transducer Datasheets

Item removed due to copyright issues. To view, refer to its source: http://www.ge-mcs.com/download/ultrasound/transducers/GEIT-20117EN_ultrasonic-transducer-catalog.pdf

Appendix B: Pulser Datasheets

Item removed due to copyright issues. To view, refer to its source:

http://www.lecoeur-electronique.net/cariboost_files/us-key_r4_0.pdf

Appendix C: MATLAB Code

Below is the MATLAB code used for processing the ultrasound scans in this work. Note that text-wrapping in this document precludes copying this code in to MATLAB without modification.

```
%% LOAD, AVERAGE, TRUNCATE AND NORMALIZE DATA

clear all; close all; clc;
path(path,'C:\Users\Jason\Documents\University\Masters_coursework\SAF\M
ATLAB');
dir =
'C:\Users\Jason\Documents\University\Masters_coursework\SAF\MATLAB\Scan
s\prf_freq_spiral4';
ang = 0:2:360;
freq = 5;
for a = 1:numel(ang)
    folder = [dir '\ang' num2str(ang(a)) '\f' num2str(freq)];
    load([folder '\uv1.mat']);
    s(a,:) = v.rec(1,:); %no averaging
    %s(a,:) = mean(v.rec,1); %average 16 scans per position
    s(a,:) = s(a,:)-mean(s(a,:));
    clear u v
end
sig = s(:,1:4000); %truncate @ end
sig = sig./std(std(sig)); %normalize

%% ALIGN SCANS

load('Alignment Shifts.mat','shifts');
for i = 2:size(s,1)
    sig(i,:) = circshift(sig(i,:),[0,shifts(i)]);
end
sig = sig(:,201:end); %truncate @ start

%% CIRCULAR DISPLAY PARAMETERS

ind_dis = 1:1000; %indexes to display
r = linspace(1,0.4,numel(ind_dis)); %[mm]
theta = pi*ang'/180;
x = cos(theta)*r;
y = sin(theta)*r;

% Display original circular image
figure; pcolor(x,y,abs(sig(:,ind_dis))); shading(gca,'interp'); axis
image
title('Original Image','FontSize',16);
set(gca,'XTick',[]); set(gca,'YTick',[]);
```

```
%% WAVELET SHRINKAGE OF LOG-SPECTRUM FOR DECONVOLUTION
%  based on:    "Blind Deconvolution of Ultrasound Sequences Using
%                Nonparametric Local Polynomial Estimates of the Pulse"

% Setting up data
S = fft(sig,[],2);
SL = log(abs(S));

%(1) Apply DWT to SL with appropriate wavelet (Symlets - near linear-
phase, near symmetric)
K = 6;% Vanishing moments - "near symmetric wavelets with vanishing
moments between 4 and 6"
M = 7;% Decomposition level - M = 3 in paper but with lower sampling
rate and fewer samples
SLW = mdwtdec('r',SL,M,['sym' num2str(2*K)]); %symN, N even, has N/2
vanishing moments

%(2) Zero-out detail coefficients and reconstruct to approximate FL
FL = mdwtrec(SLW,'a'); %reconstruct approximation coefficients

%(3) Use Hilbert transform to recover approximate F
F = exp(FL).*exp(j.*imag(hilbert(FL')'));

%(4) Apply Wiener deconvolution to approximate S/F
eps = 10000;% Wiener regularization coefficient (can be vector for
brute-force search)
blur = zeros(size(eps));
baseblur = find6dB(xcorr(reshape(abs(sig'),[],1)));
PSNR = zeros(size(eps));
basePSNR = max(max(abs(sig)))/sqrt(mean(mean(abs(sig).^2)));
cost = zeros(size(eps));
for i = 1:numel(eps)
    G = S.*F./(abs(F).^2+eps(i));
    g = ifft(G,[],2);
    g = g./std(std(g));
    blur = find6dB(xcorr(reshape(abs(g'),[],1)));%/baseblur;
    PSNR = max(max(abs(g)))/sqrt(mean(mean(abs(g).^2)));%/basePSNR;
    AWN = blur/PSNR;
    FD = Katz(reshape(g',[],1));
    entrop = imentrop(g,'r');
    cost(i) = FD; %AWN;
end
[temp,ind] = min(cost); clear temp;
G = S.*F./(abs(F).^2+eps(ind));
g = real(ifft(G,[],2));
g(abs(g)>0.7*max(max(abs(g)))) = 0.7*max(max(abs(g))); %adjust for more
effective scaling

% Display circular image
figure; pcolor(x,y,abs(g(:,ind_dis))); shading(gca,'interp'); axis
image
title(['Wiener Deconvolution - FFT Spectrum;   K = ' num2str(K) ', M =
' num2str(M) ', eps = ' num2str(eps) ...
```

```
    10 'AW&N = ' num2str(AWN) ', FD = ' num2str(FD) ', Entropy = '
num2str(entrop)],'FontSize',12);
set(gca,'XTick',[]); set(gca,'YTick',[]);

%% GABOR-TRANSFORM (STFT) LOG-SPECTRUM WAVELET SHRINKAGE

seglen = 50;
ov = 0.5;
segnum = ceil((size(sig,2)-seglen)/seglen/(1-ov)+1);

K = 6;% Vanishing moments - "near symmetric wavelets with vanishing
moments between 4 and 6"
M = 7;% Decomposition level - M = 3 in paper but with lower sampling
rate and fewer samples
eps = 10000;% Wiener regularization coefficient

gs = zeros(size(sig,1),size(sig,2),segnum);
for i = 1:segnum
    display(['progress: ' num2str(i/segnum)])
    startind = ceil((i-1)*seglen*(1-ov)+1);
    seg = sig(:,startind:startind-
1+seglen).*(ones(size(sig,1),1)*gausswin(seglen,2.15)');
    SEG = fft(seg,[],2);
    SL = log(abs(SEG));
    SLW = mdwtdec('r',SL,M,['sym' num2str(2*K)]); %symN, N even, has
N/2 vanishing moments
    FL = mdwtrec(SLW,'a'); %reconstruct approximation coefficients
    F = exp(FL).*exp(j.*imag(hilbert(FL')'));
    G = SEG.*conj(F)./(abs(F).^2+eps);
    gs(:,:,i) = [zeros(size(sig,1),startind-
1),ifft(G,[],2),zeros(size(sig,1),size(sig,2)-(startind-1+seglen))];
end
g = real(sum(gs,3));
blur = find6dB(xcorr(reshape(abs(g'),[],1)));%/baseblur;
PSNR = max(max(abs(g)))/sqrt(mean(mean(abs(g).^2)));%/basePSNR;
AWN = blur/PSNR;
FD = Katz(reshape(g',[],1));
entrop = imentrop(g,'r');
g(abs(g)>0.7*max(max(abs(g)))) = 0.7*max(max(abs(g))); %adjust for more
effective scaling

% Display circular image
figure; pcolor(x,y,abs(g(:,ind_dis))); shading(gca,'interp'); axis
image
title(['Gabor Deconvolution;   K = ' num2str(K) ', M = ' num2str(M) ',
eps = ' num2str(eps) ...
    ', seglen = ' num2str(seglen)  ',' 10 'AW&N = ' num2str(AWN) ...
    ', FD = ' num2str(FD) ', Entropy = '
num2str(entrop)],'FontSize',12);
set(gca,'XTick',[]); set(gca,'YTick',[]);

%% DWT SHRINKAGE OF LOG-CWT COEFFICIENTS AND CWT-DOMAIN WIENER
FILTERING
```

```
K = 9;% Vanishing moments - "near symmetric wavelets with vanishing
moments between 4 and 6"
M = 8;% Decomposition level - M = 3 in paper but with lower sampling
rate and fewer samples
eps = 1510;% Wiener regularization coefficient

scales = 15:40;%!note: scales not linearly related to wavelet center
frequencies!
swv = 'coif2';
swv2 = 'db2'; %****note: db2 outperforms db1 (haar) and db4
nwav = 2;

clear g
for i = 1:size(sig,1)
    display(['progress: ' num2str(i/size(sig,1))])
    S = cwt(sig(i,:),scales,swv);
    SL = log(abs(S));
    SLW = mdwtdec('c',SL,M,['sym' num2str(2*K)]); %symN, N even, has
N/2 vanishing moments
    FL = mdwtrec(SLW,'a'); %reconstruct approximation coefficients
    F = exp(FL).*exp(j.*imag(hilbert(FL)));
    switch nwav
        case 2
            F =
cwt(icwt(F,[min(scales),max(scales)],numel(scales),swv),scales,swv2);
            S = cwt(sig(i,:),scales,swv2);
            G = S.*conj(F)./(abs(F).^2+eps);
            g(i,:) =
real(icwt(G,[min(scales),max(scales)],numel(scales),swv2));
        case 1
            G = S.*conj(F)./(abs(F).^2+eps);
            g(i,:) =
real(icwt(G,[min(scales),max(scales)],numel(scales),swv));
    end
end
clc
g = g./std(std(g));
%baseblur = find6dB(xcorr(reshape(abs(sig'),[],1)));
%basePSNR = max(max(abs(sig)))/sqrt(mean(mean(abs(sig).^2)));
blur = find6dB(xcorr(reshape(abs(g'),[],1)));%/baseblur;
PSNR = max(max(abs(g)))/sqrt(mean(mean(abs(g).^2)));%/basePSNR;
AWN = blur/PSNR;
FD = Katz(reshape(g',[],1));
entrop = imentrop(g,'r');

g(abs(g)>0.7*max(max(abs(g)))) = 0.7*max(max(abs(g))); %adjust for more
effective scaling

% Display circular image
figure; pcolor(x,y,abs(g(:,ind_dis))); shading(gca,'interp'); axis
image
title(['DWT shrinkage of log-CWT;   K = ' num2str(K) ', M = '
num2str(M) ', eps = ' num2str(eps) ...
    ', scales: ' num2str(min(scales)) '-' num2str(max(scales)) ',' 10
'AW&N = ' num2str(AWN) ...
```

```
    ', FD = ' num2str(FD) ', Entropy = '
num2str(entrop)],'FontSize',12);
set(gca,'XTick',[]); set(gca,'YTick',[]);

% Print out CWT pseudo-frequencies
%display(['Pseudo-frequency range considered: '
num2str(scal2frq([max(scales),min(scales)],swv,1/160)) 'MHz'])

return

%% GENERATE THE CWT COEFFICIENT PLOT FOR USE IN THE PAPER (use averaged
scans)

swv = 'coif2';
r = 125;
S = cwt(sig(r,:),1:100,swv);

figure;
subplot(2,1,1); plot(sig(r,:)); axis tight; title('Example
Scan','FontSize',16);
xlabel('discrete-time index','FontSize',14); ylabel('recorded
signal','FontSize',14); set(gca,'FontSize',14);
subplot(2,1,2); imagesc(abs(S)); title('CWT Coefficient
Magnitude','FontSize',16);
xlabel('discrete-time index','FontSize',14); ylabel('CWT
scale','FontSize',14); set(gca,'FontSize',14);

A = 10:30;
display(['Proportion of CWT coefficients from scales ' num2str(min(A))
'-' num2str(max(A)) ' relative to scales 1-100: '
num2str(sum(sum(S(A,:).^2))/sum(sum(S.^2)))])
display(['Pseudo-frequencies in scales ' num2str(min(A)) '-'
num2str(max(A)) ': ' num2str(scal2frq(max(A),swv,1/160)) '-'
num2str(scal2frq(min(A),swv,1/160)) ' [MHz]'])
```